Collective magnetotaxis of microbial holobionts is optimized by the three-dimensional organization and magnetic properties of ectosymbionts

Daniel M Chevrier, Amélie Juhin, Nicolas Menguy, Romain Bolzoni, Paul E. D. Soto-Rodriguez, Mila Kojadinovic-Sirinelli, Greig A. Paterson, Rachid Belkhou, Wyn Williams, Fériel Skouri-Panet, et al.

Collective magnetotaxis of microbial holobionts is optimized by the three-dimensional organization and magnetic properties of ectosymbionts

Daniel M. Chevrier[1*], Amélie Juhin[2], Nicolas Menguy[2], Romain Bolzoni[1], Paul E. D. Soto-Rodriguez[1], Mila Kojadinovic-Sirinelli[1], Greig A. Paterson[3], Rachid Belkhou[4], Wyn Williams[5], Fériel Skouri-Panet[2], Artemis Kosta[6], Hugo Le Guenno[6], Eva Pereiro[7], Damien Faivre[1], Karim Benzerara[2], Caroline L. Monteil[1], Christopher T. Lefevre[1*]

[1]Aix-Marseille Université, CNRS, CEA, UMR7265, BIAM, Saint-Paul-lez-Durance 13108, France

[2]Sorbonne Université, UMR CNRS 7590, MNHN, IRD, Institut de Minéralogie, de Physique des Matériaux et de Cosmochimie, IMPMC, 75005, Paris, France

[3]Department of Earth, Ocean and Ecological Sciences, University of Liverpool, L69 7ZE, Liverpool, UK

[4]Synchrotron Soleil, L'Orme des Merisiers, Saint-Aubin -BP 48, 91192 Gif-sur-Yvette Cedex, France

[5]University of Edinburgh, School of GeoSciences, Grant Institute, West Mains Road, Edinburgh EH9 3JW

[6]Plateforme de Microscopie de l'Institut de Microbiologie de la Méditerranée, IMM, Institut de Microbiologie, FR3479, Campus CNRS, 13402 Marseille cedex 20, France

[7]ALBA Synchrotron Light Source, Cerdanyola del Vallés, Barcelona 08290, Spain

***Corresponding authors**: Drs. Daniel Chevrier and Christopher T. Lefevre

Emails: daniel.chevrier@cea.fr and christopher.lefevre@cea.fr

ORCID: Daniel M. Chevrier (0000-0002-0914-6714), Amélie Juhin (0000-0003-0752-3034), Nicolas Menguy (0000-0003-4613-2490), Romain Bolzoni (0000-0002-5741-3856), Paul E. D. Soto-Rodriguez (0000-0002-2425-932X), Mila Kojadinovic-Sirinelli (0000-0001-8110-3113), Greig A. Paterson (0000-0002-6864-7420), Rachid Belkhou (0000-0002-2218-7481), Wyn Williams (0000-0001-9210-7574), Fériel Skouri-Panet (0000-0002-2623-9058), Artemis Kosta (0000-0001-7115-4566), Hugo Le Guenno (0000-0003-1768-1212), Eva Pereiro (0000-0001-7626-5935), Damien Faivre (0000-0001-6191-3389), Karim Benzerara (0000-0002-0553-0137), Caroline L. Monteil (0000-0002-2834-6834), Christopher T. Lefevre (0000-0002-1692-0245).

Author contributions: D.M.C., A.J., N.M., D.F. K.B., C.L.M., and C.T.L. designed research; D.M.C., A.J., N.M., K.B., Ro.B., W.W., G.A.P., M.K.S., P.E.D.S.R., and C.T.L. performed research; F.S.P., Ra.B., D.F., A.K., H.L.G., and E.P. contributed new reagents/analytic tools; D.M.C., A.J., N.M., K.B., P.E.D.S.R. and C.T.L. analyzed data; D.M.C., C.L.M., and C.T.L. wrote the paper; N.M., P.E.D.S.R., G.A.P., D.F. and K.B. contributed partial writing.

The authors declare no competing interest.

Classification: Biological Sciences (Major), Biophysics and Computational Biology (Minor)

Keywords: collective magnetotaxis, magnetosomes, symbiosis, biomineralization, holobiont, magnetotactic bacteria

Abstract

Over the last few decades, symbiosis and the concept of holobiont – a host entity with a population of symbionts – have gained a central role in our understanding of life functioning and diversification. Regardless of the type of partner interactions, understanding how the biophysical properties of each individual symbiont and their assembly may generate collective behaviors at the holobiont scale remains a fundamental challenge. This is particularly intriguing in the case of the newly discovered magnetotactic holobionts (MHB) whose motility relies on a collective magnetotaxis (*i.e.*, a magnetic field-assisted motility guided by a chemo-aerotaxis system). This complex behavior raises many questions regarding how magnetic properties of symbionts determine holobiont magnetism and motility. Here, a suite of light-, electron- and X-ray-based microscopy techniques (including X-ray magnetic circular dichroism (XMCD)) reveals that symbionts optimize the motility, the ultrastructure and the magnetic properties of MHBs from the microscale to the nanoscale. In the case of these magnetic symbionts, the magnetic moment transferred to the host cell is in excess (10^2-10^3 times stronger than free-living magnetotactic bacteria), well above the threshold for the host cell to gain a magnetotactic advantage. The surface organization of symbionts is explicitly presented herein, depicting bacterial membrane structures that ensure longitudinal alignment of cells. Magnetic dipole and nanocrystalline orientations of magnetosomes were also shown to be consistently oriented in the longitudinal direction, maximizing the magnetic moment of each symbiont. With an excessive magnetic moment given to the host cell, the benefit provided by magnetosome biomineralization beyond magnetotaxis can be questioned.

Significance Statement

Symbiosis between a motile microeukaryotic host and dozens of non-motile, surface-attached magnetic bacterial symbionts was recently discovered, where the host acquires geomagnetic field-guided navigation thanks to chains of ferrimagnetic nanoparticles (within organelles called magnetosomes) produced by the bacteria. Our findings reveal magnetic dipoles of each magnetosome chain consistently align and thus efficiently confer a large magnetic moment to the host cell. Remarkably, the calculated magnetic moment is greatly in excess of that required to gain a magnetotactic advantage. These results show an optimization

of collective magnetotaxis during the course of evolution owing to the three-dimensional organization and magnetic properties of bacteria but also raise the question on the magnetosome's function beyond magnetic field guidance since they abundantly cover the host.

Introduction

Species are adapted to their environment thanks to the heritable changes in their structure, physiology, locomotion, dispersal, reproduction and other behaviors that have passed the filter of natural selection over generations. Several evolutionary forces may trigger these changes and shape biodiversity, among which symbiosis has gained a lot of recognition in recent decades (1). By creating intimate and long-term physical interactions, different organisms may rapidly acquire a variety of functions, ranging from detoxification, to cell defense, motility and, in most cases, metabolic abilities. Together, symbiotic microorganisms form a single ecological unit, called a holobiont (2), whose functioning allows its partners/bionts to extend their ecological niche and colonize otherwise previously inaccessible habitats. The symbiont integration level may vary from a simple attachment to cell surfaces to their integration into the cell cytoplasm. In the most extreme cases of endosymbiont host integration, symbiosis can even lead to the creation of new organelles and genome transfer to the host nucleus, often illustrated by the eukaryogenesis (3, 4).

Symbioses are established between organisms from all domains of life and have been mostly studied in macrobial systems involving multicellular eukaryote models (5, 6). Symbioses in the microbial world are also widespread but less known even though they are of prime interest to gain insights into the mechanisms driving life complexification and evolution. However, observation and characterization of microbial symbioses have been challenging for many years; most symbionts defy commonly applied enrichment and cultivation techniques (1). Even if metagenomic and single-cell genomic approaches may now circumvent some of these issues by enabling the reconstruction of genomes from symbionts in their natural habitats (7), *in silico* approaches do not entirely reveal the holobiont structure and behavior. Therefore, interrogating the physical properties of microbial symbiotic systems may bring insights on mechanisms or interactions that have shaped biodiversity. Improvements in micro- and nano-scale analytical instrumentation and sample preparation strategies over the past few years have boosted biophysical research, permitting microbial holobiont studies from the single cell level to organelle level (8). For instance, approaches such as synchrotron-based X-ray spectromicroscopy imaging, focused ion beam (FIB)-scanning electron microscopy, and cryo electron microscopy (and associated cryo-preparation protocols) have made it possible to rigorously examine the ultrastructure and organization of individual

cells, while other techniques such as nanoscale secondary ion mass spectrometry (NanoSIMS) can trace the metabolic exchanges to decipher intra-/inter-cellular chemical interactions (9).

Microbial holobionts may adopt behavior patterns almost completely determined by the symbionts. Cell to cell interactions between bionts generate an emergent collective behavior that may change the mechanical, biological and physicochemical properties of each partner over generations. Although debated amongst evolutionary biologists (10, 11), a microbial holobiont can nevertheless be seen as a main unit of selection. As such, any cell or organelle function, structure and organization optimizing the collective behavior may therefore be selected in a given environmental context. These evolutionary processes may create a complete dependency in some biological systems, which is well illustrated by mitochondria and chloroplast evolution (12). Not all symbioses are obligatory, but most of them involve a metabolic dependency from at least one of the partners. Such is the case with the endosymbiotic methanogenic archaea or denitrifying bacteria in hydrogenosome-bearing protists (13, 14). Other benefits can rely on structural integrity or locomotion. Indeed, similar to other biological systems (15), symbiont interactions can generate a collective motion. For example, some flagellates are mobile owing to thousands of ectosymbiotic bacteria (*e.g.*, spirochetes) anchored to the host membrane, which ensure its movement with their flagella (16).

Recently, a new collective behavior was described in a group of microbial holobionts ubiquitous in anoxic marine sediments. The functioning of this holobiont relies on a multi-scale cooperation between a flagellate, euglenozoan protist and dozens of non-flagellated, sulfate-reducing bacteria of the *Deltaproteobacteria* class, which biomineralize magnetic nanocrystals (17). First, the host and symbionts interdependency relies on metabolic exchanges. Some of them were identified based on the host ultrastructure and ectosymbiont genome (17). Their syntrophy is most likely based on the transfer of molecular hydrogen produced by mitochondria-derived organelles, called hydrogenosomes, from the host to the bacteria that use it to reduce sulfate. Second, these holobionts harbor a peculiarity compared to other symbiotic systems described in such habitats: they adopt a collective magnetotaxis, (*i.e.*, a motility guided by a chemo-aerotaxis system and geomagnetic fields). Similar to magnetotactic bacteria (MTB) (18, 19), magnetotactic holobiont (MHB) motility is guided by geomagnetic fields, which is assumed to facilitate their positioning in preferred ecological niches, just below the oxic-anoxic boundaries of sediments. The passive alignment in a magnetic field is ensured by ectosymbionts through the biomineralization of chained lipidic vesicle-encapsulated ferrimagnetic nanocrystals called magnetosomes. Experimental observations evidenced that the magnetic guidance was influenced by oxygen gradients, while a nearly complete genome of biomineralizing bacteria showed complete loss of sensing and motility machinery (17). Therefore, magnetotaxis appears to emerge from the collective effects of magnetosome chain positioning from ectosymbiotic bacteria and the host motility and chemo-aerotaxis.

The discovery of MHBs raises many questions regarding the magnetic properties of this collective behavior and how it echoes the magnetic properties developed in free-living prokaryotes (*i.e.*, MTB). As long as magnetotaxis provides a selective advantage (20), the function is supposed to have been optimized over the time of holobiont diversification. If so, to what extent did holobionts converge toward the same motility behavior in response to chemical gradients and magnetic fields as in prokaryotes? And since cell polarity, flagella organization, magnetosomes arrangement, number and polarity impact magnetic behavior in free-living MTB (21–25), how are these features organized by symbionts to maintain a successful magnetic guidance at the scale of the consortium?

Here, we employ light-, electron- and X-ray-based microscopy techniques to characterize the motility, the ultrastructure and the magnetic properties of MHBs. The calculated magnetic dipole of MHBs from magnetic field-based motility assays was found to be more than two orders of magnitude greater than free-living MTB, an amount clearly in excess of that required to gain a magnetotactic advantage. Microscopy imaging of MHB ultrastructure (using scanning electron microscopy (SEM), transmission electron microscopy (TEM), scanning-TEM (STEM), cryo soft X-ray tomography (cryo-SXT)) and spectroscopic investigation of magnetosome magnetic properties (using X-ray magnetic circular dichroism (XMCD)) confirm a cohesive organization of ectosymbiotic cells and consistent magnetic dipole direction of magnetosome chains relative to the host, which confers an ultrasensitive magnetotaxis property to the holobiont. Lastly, unlike previously reported magnetite (Fe_3O_4) crystal morphology in *Deltaproteobacteria*, we discovered that ectosymbiotic bacteria produce rhomboidal dodecahedron-like particles. From the microscale to the nanoscale, the results support hypotheses that the positioning, organization and number of ectosymbiotic cells and magnetosome chains are overly optimized by symbionts to insure a collective magnetotaxis similar to the magnetotaxis behavior observed in MTB. Furthermore, these results stimulate the debate of magnetosomes function beyond magnetotaxis since the additive magnetic moment is orders of magnitude in excess of that required for effective magnetotaxis.

Results

Magnetotactic holobionts have a magnetotactic behavior similar to free-living magnetotactic bacteria

Since the first description of magnetotactic holobionts (MHBs) (17), we have continuously collected samples in Carry-le-Rouet, France (Mediterranean Sea), to have a sufficient number of south-seeking MHBs to perform an extensive characterization of their ultrastructure and magnetotaxis. SEM and light microscopy observations show two thick flagella, each measuring about two to three times the length of the cell body, which is typical in Euglenids (Movie S1 and Fig. 1A). Transverse section of the flagella shows a canonical '9+2' microtubule axoneme structure (Fig. S1) (26). SEM and TEM indicate that both flagella emerge from a large depression (Fig. 1) from the anterior pole where the protist is only partially covered by few magnetic ectosymbiotic bacteria (MEB) in contrast to the rest of its cell body (Fig. 1D and E). SEM observations at low electron energy show magnetic ectosymbiotic bacteria (MEB) densely cover the surface of the protist (Fig. 1B), while imaging at higher electron energy confirmed that they contained structurally-aligned nanoparticle chains (Fig. 1C).

We assessed the extent to which collective magnetotaxis evolved towards the same motility behavior as the one observed in single-celled MTB. Magnetic moments of MHBs were obtained by analyzing their U-turn motion (Fig. 2A and B present optical image of MHB in recorded video and schematic of U-turn experiment, Fig. S2 presents additional extracted motility parameters), which relates the radius and turning time of MHBs upon external magnetic field reversal using the following equation (27):

$$\tau_{Uturn} = \frac{A}{M \cdot B} \cdot \ln\left(\frac{2 \cdot M \cdot B}{k_B T}\right) \qquad (1)$$

Here, τ_{Uturn} corresponds to the time the MHB take to make a U-turn upon switching the applied magnetic field (B); M is the magnetic moment of the MHB; k_B corresponds to the Boltzmann constant and T the temperature at which the experiment was performed (25°C). A is a constant related to a viscous torque. By considering the MHB shape to be an ellipsoid (17), it is defined as:

$$A = \left(\frac{16}{3}\right)\pi\eta c^3 \cdot \left[\frac{1}{2} \cdot ln\left(\frac{(a+c)}{(a-c)}\right) - \frac{(a*c)}{b^2}\right] \qquad (2)$$

Where η corresponds to the media viscosity (*i.e.*, Mediterranean Sea viscosity at 25 °C), a (10 µm) and b (5 µm) are the major and minor axes of the ellipsoid, respectively, and $c^2 = a^2 - b^2$. The MHB U-turn time (τ_{Uturn}) was determined by tracking the U-turn trajectory and then plotting the first derivative,

corresponding to the instantaneous velocity (Fig. 2C), where the change in sign corresponds to the change in direction. Then, by taking the time difference between maximum and minimum peaks (shown in Fig. 2D), the value of τ is obtained and therefore M can be calculated from equation (1). A set of MHB U-turn trajectories (n = 22) were tracked to calculate τ_{Uturn} and M. We obtained an average absolute value of the magnetic moment $M = 1.8 \pm 0.8 \times 10^{-13}$ A·m^2. Similar magnetic moments have been found for *Candidatus* Magnetoglobus multicellularis (between $9 \pm 2 \times 10^{-15}$ and $20 \pm 3 \times 10^{-15}$ A·m^2 (28)) and magnetotactic protists (6.7×10^{-12} A·m^2 (29) and $2.5 \pm 1.2 \times 10^{-13}$ A·m^2 (30)). As a comparison, the magnetic moment of *Magnetospirillum gryphiswaldense* (MSR-1) was previously determined to be $2.5 \pm 0.5 \times 10^{-16}$ A·m^2 (31) or around 7.7×10^{-16} A·m^2 by direct measurement of the magnetosome chain using magnetic tweezers (32). Similar magnetic moments have been found for other species of MTB as well (33, 34).

Ectosymbiotic cells are parallel to each other and oriented along the long axis of their protistan host

To obtain a global understanding of MEB organization in their native-state configuration (*i.e.*, without congealing artifacts from fixation processes), MHB samples were vitrified for cryo soft X-ray tomography (cryo-SXT) imaging. Cryo-SXT offers a relatively deep penetration and enhanced natural contrast of biological materials in the water window (*i.e.*, X-ray absorption from C and N K-edges) without chemical fixation or staining. Fig. 3A presents tomogram reconstructed slices of the vitrified MHB captured with an incident energy of 520 eV (raw X-ray image of this MHB and tilt-series images are shown in Fig. S3, see Movie S2 for tomogram video). Owing to a voxel size of $(12\ nm)^3$ and the high density of magnetite nanocrystals, magnetosome chains were distinguishable in MEB from tomography virtual slices and were assigned during volume segmentation (see Materials and Methods). The segmentation of the entire volume reconstruction is presented in Fig. 3B with magnetosome chains in red, MEB membrane in yellow (only partially reconstructed due to limited contrast in the tomographic volume), protistan host in cyan (*i.e.*, outer membrane and intracellular compartments) and dense intracellular granules in white (identified as phosphorus- and calcium-rich granules using X-ray energy-dispersive spectrometry (XEDS); Fig. S4). The bottom side of the MHB (in contact with the carbon film of TEM grid) was flattened likely due to sedimentation or the vitrification process. This can be observed from the "front" and "side" views of the reconstructed model (Fig 3B, right panels). When considering the magnetosome chains in red; Fig. S5 shows only this reconstructed volume and the protistan host. We note the magnetosome organization has a general similarity to that identified with multicellular magnetotactic prokaryotes (MMPs) (35, 36); magnetosomes are found at the exterior of the consortium and they align in the direction from pole to pole. For MMPs, however, magnetosomes organize into chain-like clusters, not distinct chains as for the MHB.

Thin-sections of MHB confirmed that the protistan host is covered by one layer of longitudinally arranged, curved rod-shaped ectosymbiotic bacteria (Fig. 1D and 4A and B). Bacterial cells are localized within an invagination of the outer membrane of their host (Fig. 4A-C). Such channel-like structures may help the bacteria to maintain position at the surface of the eukaryotic host and increase their surface contact with the host for increased transfer of material for chemical symbiosis-related exchanges. Transversal sections of ectosymbionts revealed a consistent and unique morphology (Fig. 4A-E). As previously reported (17), transversal sections indicate the presence of wing-like structures in all ectosymbionts. Here, we show that these structures are protrusions from the external membrane only (Fig. 4C-E) with one of the wing structures often below and the other above neighboring bacterial cells (Fig. 4D). These structures could also be observed from SEM images where they appear as tapered edges (Fig. S6). The linking of adjacent wing structures may help to improve ectosymbiotic cells cohesion. Longitudinal and transversal sections also reveal the presence of vesicles (*i.e.*, round structures) between bacteria that could also be involved in the fixation of the symbionts (Fig. 4c-f). These vesicles could also be part of the communication between MEB to coordinate their activities such as cell division. Similar to the vesicles previously observed in MMPs (21). The presence of the ectosymbiotic bacteria in the vicinity of hydrogenosomes produced by the protist was also confirmed (Fig. 4C and D).

Transversal sections indicate that magnetosomes are always positioned in the lower half of the MEB cell body, closer to the host (Fig. 4A-E) or on side of the MEB with shorter inner curvature radius. Similar magnetosome positioning at midcell was previously reported in the free-living *Magnetospirillum gryphiswaldense* MSR-1. It was shown that the cytoskeletal determinant CcfM links the magnetoskeleton (*i.e.*, magnetosome-specific cytoskeleton produced by specific proteins such as MamK) to cell morphology in regions of inner positive-cell curvature (22). In the case of MEB, such positioning of the magnetosome chain could represent an advantage for optimizing the magnetic moment of the MHB. Although the genome of MEB did not contain any orthologue of CcfM, it is possible that another molecular pathway is involved in magnetosome positioning in MHBs.

All magnetosome chains are aligned along the long axis of the host cell. Towards the front or back of the host, magnetosome chains are tilted inward (*i.e.*, following the curvature of the host cell), indicating a close contact between MEB and the surface of the host cell. From cryo-SXT volume reconstruction (Fig. 3) and TEM thin sections (Fig. 4), parallel magnetosome chains are typically spaced 0.5-1 µm apart. Considering the potential for interchain interactions to influence the ensemble magnetic properties, micromagnetic calculations of simulated magnetosome chain structures were conducted using MERRILL (v1.6.4) (see Materials and Methods) (37). Based on the average particle size, spacing and number of particles per chain as measured by TEM, a chain of 25 rhomboidal dodecahedral nanocrystals (see section

below for the characterization of the nanocrystal shape) with a mid-sphere diameter of 60 nm and 10 nm spacing between grains was built to model the adjacent stray fields. Based on this calculation (Fig. S7), stray fields at least 1 μm from the chain (in both parallel and perpendicular directions) are consistently more than three orders of magnitude weaker than the remnant magnetization (M_{rs}) of the entire chain (8.4×10^{-16} $A \cdot m^2$, see Materials and Methods), ruling out significant interchain interactions. Moreover, the magnetic moment for one of the modelled magnetosome chain structures is high enough to overcome Brownian motion at 20 °C in a magnetic field of 10 μT. To impart a magnetotactic advantage for MHBs over other microorganisms of similar size (*i.e.*, a net average bias (> 50 % of the population) of *n* cells aligned with the magnetic field direction against randomized orientation caused by Brownian motion), we considered how the magnetic moment of magnetosome chains decrease because of their bending to follow curvature of the host cell (Fig. S8). Regardless of these few chains at the extreme ends of the cell, which are highly curved, we estimate that net cell magnetization from only a few chains positioned close to the middle section of the host is sufficient to confer magnetotaxis on the MHB (see Fig. S8 and Materials and Methods). The total magnetic moment of the holobiont being 1.8×10^{-13} $A \cdot m^2$ and that of a single magnetosome chain 8.4×10^{-16} $A \cdot m^2$, with most of the magnetosome chains aligned parallel to each other, our model would indicate there are about 215 chains attached to the host which is consistent with microscopy observation (100-200 MEB/holobiont) (17).

Magnetic moments of magnetosome chains align to enhance magnetotaxis ability of their host

Considering magnetosome chain organization, negligible interchain interaction, and the above-calculated ensemble magnetic moment of MHBs, the magnetic moment of each chain should contribute independently and additively to the magnetic moment the host cell experiences. This assumption was tested by measuring the native-state magnetic moment of individual chains *via* scanning transmission X-ray microscopy with X-ray magnetic circular dichroism (STXM-XMCD) in the absence of applied magnetic fields.

For STXM-XMCD sample preparation, MHB samples were magnetically extracted from environmental samples using weak magnetic fields (see Materials and Methods). Further, when collecting XMCD, no magnetic fields were applied on the sample. Instead, the sample was tilted ~30° to the normal plane to probe the intrinsic magnetization of each magnetite nanocrystal (Fig. S9A and B for experimental setup) (38). MHBs with magnetosome chains positioned perpendicular to the axis of rotation of the sample holder were analyzed to optimize the XMCD signal. This is because the magnetization easy axis is typically aligned along the magnetosome chain direction, *i.e.*, <111> crystallographic direction of magnetite (see below for high-resolution TEM analyses; (39–41)). Furthermore, it was important to identify MHBs that

had intact flagella, so that a correlation between the magnetization of magnetosome chains and the swimming direction (*i.e.*, south-seeking) could be assessed.

Fig. 5A and B present STXM images of two different MHBs positioned in opposite directions and observed at 710 eV (*i.e.*, at the Fe L_3-edge), where magnetosome chains are most visible against the host cell. At this energy, it is also possible to observe the flagella of the deposited MHBs (confirmed with optical microscopy). We then utilized three energy points in the Fe L_3-edge absorption region that show the maximum XMCD response (708.8, 709.8 and 710.7 eV, see Fig. S9C for identification of these energies) to collect maps with both circular polarizations of incident X-rays (circular polarized left (CPL) and right (CPR)). Higher resolution analyses on regions of interest for the first MHB show differences in signal intensity between circular polarizations (Fig. 5C). Based on the tilt direction of the sample holder, the orientation of MHB (*i.e.*, swimming direction) and the circular polarization, the resulting color in the XMCD difference maps indicates the direction of magnetization. Here, the red color indicates magnetization in the right direction (Fig. 5C), while blue indicates magnetization in the left direction (Fig. 5D). As seen from the presented XMCD difference maps, the projected magnetization of magnetosome chains is mostly uniform, pointing towards the flagella end of the MHB. This was confirmed by measuring another MHB with the flagella on the opposite side (Fig. 5B and D). In total, three MHB were analyzed (Fig. S10 shows the third MHB without chemical fixation), consistently demonstrating magnetic dipoles of magnetosome chains are in the same direction among ectosymbionts with their magnetic south pole pointing toward the flagella, thus optimizing the swimming direction of the protistan host toward the south. This suggests magnetic dipole direction is maintained for dividing ectosymbionts. A similar conservation of magnetic dipole direction relative to consortium structure during division has also been identified for multicellular magnetotactic prokaryotes (MMPs) (42).

An inversion of individual magnetic dipole direction against the overall magnetization vector was discovered on a few occasions, which occurs in the middle or at the end of magnetosome chains. These inversions are evident by the alternating red-blue regions in the CPL-CPR difference maps (Fig. 5C). These inversions also confirm the magnetic field strength used to extract MHBs from collected sediment did not disturb native magnetic moments of magnetosomes. The crystalline orientation of magnetosome particles in one inversion region was revisited and examined using scanning transmission electron microscopy high-angle annular dark field (STEM-HAADF) imaging. Fig. S11 shows the STXM region in Fig. 5A (top left region, purple frame) and plots the <111> alignment of individual particles as found from FFT and stereographic projections. This demonstrates the consistent alignment of magnetite's easy axis <111> with the chain direction despite the inversion of magnetic dipoles.

We then performed further HR-TEM analyses of individual magnetosomes for three MEB from three different MHBs, confirming expected {111}, {100} and {110} faces of magnetite nanocrystals (Fig. 6) and identifying the nanocrystal orientation in chain structures. The <111> crystallographic direction of each particle was almost systematically aligned along the chain length. This is consistent with the orientation generally observed for individual MTB biomineralizing prismatic magnetite (41). Upon close inspection of several individual magnetosomes, the shape of most magnetite nanocrystals is best described as a rhomboidal dodecahedron (Fig. S12 and S13), a morphology that exhibits only {110} faces. Fig. S14 and S15 present additional HR-TEM analyses of individual particles and demonstrate the consistent <111> alignment with chain direction and further this unexpected nanocrystal shape for magnetite. This crystallographic form of magnetite from a magnetosome-producing bacterium of the *Deltaproteobacteria* class is unanticipated, which suggests previous studies that correlated the nanocrystal morphology formed by a bacterium and its phylogenetic position should be reconsidered (41, 43, 44).

Discussion

Many microorganisms, including bacteria, microeukaryotes and archaea, live together permanently or at least transitorily by forming microbial holobionts. These intimate relationships must not only satisfy metabolic requirements, but their physical assembly must maintain, and even improve, holobiont integrity and motion. This study utilized a suite of imaging and characterization tools to generate insights on one of the most fundamental cases of collective magnetotaxis known, ranging from motility in magnetic fields, three-dimensional organization of magnetosome chains around the host cell, polarity of magnetic dipoles, ultrastructure of bacterial cells at the surface of the host, down to the morphology of magnetite nanocrystals. Based on the different scales of our analysis, the MHB studied here is a model system apt to be investigated with the electron and X-ray based imaging, which provide the adequate spatial resolutions to capture the intricate organization at both cellular and nanoparticle size regimes. Based on MHBs, what can symbiosis research gain from such collective motion and physical characterization studies?

The first finding is that a similar field-guided motility has emerged independently in free-living single-celled MTB and in microeukaryotes through symbioses, although the magnetosome organelle has a common prokaryotic origin. The magnetic moment determined using U-turn analysis was $1.8 \pm 0.8 \times 10^{-13}$ $A \cdot m^2$ (n = 22), a value more than two orders of magnitude higher than the magnetic moment of a single MTB (45–49). This magnitude of magnetic interaction with the geomagnetic field is in excess for the MHB. Our micromagnetic calculations on the magnetic dipole strength of simulated magnetosome chains and the

size and shape of the entire holobiont estimate (considering Brownian motion at 20 °C) that only a few magnetosome chains – not dozens – positioned longitudinally along the mid-section of the host cell would be sufficient for the protist cell to gain a magnetotactic advantage (in fields > 10 μT) over other motile microorganisms of similar size (see Fig. S8 and Materials and Methods). It was then hypothesized from this calculation and our characterization of the MHB that perhaps more magnetosome chains were necessary during periods of weak geomagnetic field strength in Earth's history. However, even with a field strength of ~1 μT, only a few additional magnetosome chains contributing to the additive magnetic moment of a holobiont would be required (Fig. S8). Therefore, the dozens of magnetosome chains that cover the MHB are greatly in excess of what is required for effective magnetotaxis. Similar observations have been made in the magnetotactic multicellular prokaryotes where their magnetic moment was optimized to a large degree (28, 36, 42).

At the magnetosome level, we observed a uniformity of magnetic dipole direction in MEB. However, as presented in Fig. 5C, inversion of magnetosome magnetic dipole was detected on a few occasions, although its origin could not be determined by the present work. We note that magnetic dipole inversions have been reported for MTB strains MV-1 and AMB-1 when a similar XMCD-STXM measurement was performed (38, 50). In the case of *Magnetospirillum magneticum* (AMB-1) studies, inversion of an entire magnetosome chain segment was found for a mature cell, whereas out-of-plane magnetic dipoles were found for recently biomineralized magnetosomes. For MHB, the alternating inversions of individual magnetosomes do not appear to originate from immature magnetosomes as these particles are found mid chain, spaced closely to other magnetosomes, and are of average particle size. Regardless of this irregularity to be further understood, the consistent alignment of chain magnetic dipoles is an indicator of highly controlled cell division (24) and appropriation of chains on the host cell to maintain the maximum magnetic moment. This is in contrast to a recent finding by Leão *et al.* (30) where bundles or clusters of bullet-shaped magnetosomes were discovered in a flagellated protist that showed a seemingly random organization of magnetosome magnetic dipoles.

TEM examinations reveal additional interesting features: bionts have evolved specific structures and three-dimensional organization to optimize holobiont stability and hydrodynamics. Chains and MEB cells are parallel to the microeukaryote/holobiont motility axis, and extracellular vesicles and MEB wing-like protrusions seem to stick and arrange bionts together in this orientation. This reveals that beyond the chemical symbiosis previously described between host and ectosymbiotic bacteria (17), the holobiont collective behavior emerges from physical interactions between biological interfaces (positioning and structural integrity of ectosymbiotic bacteria on the host) and between magnetic dipoles and the geomagnetic field (retention of magnetic dipole direction with respect to direction of motility). These

physical constraints may act on biology to drive the adaptive evolution of the holobiont. Without complying to these physical restrictions, the consortium's persistence would be challenged.

Such a biological constraint exerted by magnetotaxis suggests an important ecological role for the holobiont. As hypothesized previously (17), the host benefits from the same advantages as MTB in chemical gradients, namely, finding more easily optimal chemical redox conditions in fluctuating environments. Collective magnetotaxis may thus optimize holobiont efficiency for nutrient acquisition or avoidance of toxic substances. Sharing the function with the protistan host may avoid the metabolic burden of synthesizing flagellar components for MEB, the energetic expense of fueling flagellar motors and the exposure of some molecules that could be recognized by predators. More environmental and genomic data will resolve the adaptive history, but can the biophysical characterization of MHBs give insights into the syntrophy itself or the fundamental role of magnetosomes in MTB? Attention has been paid to the geolocation function of magnetosomes to explain the emergence of such a biomineral and organelle (43, 51, 52). However, if this primary function requires only few magnetosome chains in MHBs, then why is the magnitude of magnetic interaction with the geomagnetic field excessive, and why do MEB continue to spend energy to produce such an excess number of magnetosomes? Here, MHBs provide further evidence that magnetosomes might also be involved in metabolic aspects and possibly syntrophy. Similar to what has been proposed for MTB, MEB could act as a battery to fuel the protist (53). The close vicinity of magnetosomes to the protist's external membrane could evidence a possible traffic of energy from prokaryotic cells toward the eukaryotic host, similar to how hydrogenosomes function but in the opposite direction (*i.e.*, fueling the MEB with H_2) (17, 54). Another hypothesis explaining such a large amount of magnetosomes in MHBs is an antioxidant defense. Indeed, it was shown in model MTB strains of the *Magnetospirillum* genus that magnetosomes exhibit a peroxidase-like activity (55, 56). Magnetosomes were proposed to decrease and eliminate reactive oxygen species (ROS) in the cell. Thus, in MHBs, ectosymbiotic cells could serve as a sink for the ROS produced by their protistan host during metabolic activity or exposure to oxygen (57). Although little is known about the physiology of this MHB protist and its closest relatives, it is possible that they require a high concentration of iron for metabolic needs. Since MTB are known to be very efficient in the uptake of iron (58), the protist could benefit from the iron uptake by its symbionts with the transfer of iron from the ectosymbionts toward the protist.

Magnetotaxis in MTB is usually described as a passive orientation and active swimming along the Earth's magnetic field lines thanks to magnetosomes and to flagella, respectively (59). However, it was shown that a potential magnetic sensing, *via* the widely used chemotaxis mechanism, might be actively involved in magnetotaxis (60). In *Magnetospirillum magneticum* AMB-1, a methyl-accepting chemotaxis protein (MCP) appears to interact with the protein MamK involved in magnetosome chain formation. This finding led to the hypothesis that the magnetic torque applied on the magnetosome chain might be relayed

by MamK and transferred to MCPs at the cell poles *via* specific interactions between them. The chemotaxis signal transduction system may then take over the subsequent response of the cell. In MHBs, it is likely that such signal transduction system between the MEB magnetosome chains and the host flagellar motor is absent as it was shown that none of the genes encoding classical chemotaxis pathways were detected in the genome of MEB (17). Thus, to overcome potential swimming deviation against the Earth's magnetic field, a last hypothesis to consider is that the higher the number of magnetosome chains, the better MHBs can maintain a swimming direction parallel to the magnetic field.

Future studies that inspect MHBs under laboratory-based conditions and their diversity in aquatic environments will hopefully reveal more on the function of magnetosomes for eukaryotes. The discovery of collective magnetotaxis has opened up a new interdisciplinary field of study in biology and biophysics to answer the questions this symbiosis between eukaryotes and prokaryotes generates on their evolution (*i.e.,* were ectosymbiotic bacteria originally recruited with the ability to produce magnetosomes or was the formation of magnetosomes acquired by the bacteria after they started their symbiosis with their host?) and functioning (*i.e.,* what major advantages does the protist obtain by carrying dozens of biomineralizing bacteria on its surface?).

Materials and Methods

Sample collection and light microscopy observations. Samples were collected by free-diving at a water depth of 0.5-2 m in the Mediterranean Sea, in Carry-le-Rouet (43.334222°N, 5.175278°E). One-liter glass bottles were filled to about 0.3-0.5 of their volume with sediment, then filled to their capacity with water that overlaid the sediment. Air bubbles were excluded. Once in the laboratory, samples were stored under dim light at room temperature (~ 25 °C). South-seeking magnetotactic holobionts were concentrated by placing a magnetic stirring bar (~ 10 mT) next to the bottles, above the sediment-water interface for 2 h. Examination of magnetically concentrated cells was carried out using the hanging drop technique (61) under a Zeiss Primo Star light microscope equipped with phase-contrast and differential interference contrast optics. The local magnetic field used to determine magnetotaxis was reversed by rotating the stirring bar magnet 180 ° on the microscope stage.

Movement and magnetotactic response analysis. A customized magnetic microscope equipped with a triaxial Helmholtz coilset and controller (C-SpinCoil-XYZ, Micro Magnetics Inc.) and a Andor Zyla 5.5 high speed camera was used (62). The 3D-axis Helmholtz coils can generate DC magnetic fields with a precision of 5 % of Earth's magnetic field (± 2.5 µT). Using the setup, we programmed the switching of

the magnetic field between -3.5 and +3.5 mT for the U-turn. For U-turn measurements, the magnetic field was fixed for 2 s before switching. The switching was repeated to collect at least three U-turns in the field of view. The trajectories and U-turn of 22 MHB were extracted and smoothed by a tracking script written in python and based on the OpenCV Object Tracking Algorithms with the CSRT tracker. The data is smoothed by a convolution-based smoothing approach. For both trajectory and U-turn measurements, a 20X objective (N.A. 0.45) was used. The mathematical relation to calculate the MHB magnetic moment from the U-turn time are described in the main text by equations (1) and (2). The fsolve function from Octave/Matlab was used to obtain *M* from equation (1). Data fitting was done by the intrinsic fitting functions of OriginPro, Version 2016 (OriginLab Corporation, Northampton, MA, USA).

Scanning electron microscopy (SEM). Magnetically concentrated MHB were fixed in a solution of 1 % paraformaldehyde and deposited on a glass coverslip coated with poly-L-lysine and stored at 4 °C. Before the observation, the sample was dehydrated in successive ethanol baths (50 %, 70 %, 96 %, 100 %) then processed through critical point drying (CPD) (Leica EM CPD300) before coating with carbon (Leica EM SCD500). Images were collected in the backscattered and secondary electron modes using a Zeiss Ultra 55 FEG-SEM operating at 1–10 kV, a working distance of 4 mm and an aperture of 10–60 μm.

Transmission electron microscopes (TEM). TEM was used on ultrathin sections to characterize the ultrastructure of the magnetotactic holobionts. Thin-sectioned samples were prepared from magnetically concentrated protists fixed in 2.5 % (w/v) glutaraldehyde in sodium cacodylate buffer (0.1 M, pH 7.4) and kept at 4 °C for at least 24 h. Due to the low biomass of MHB, fixed cells were embedded in a small agarose plug to facilitate their transfer in the different solutions before the inclusion in resin. Cells were post-fixed one hour with 1 % (w/v) of osmium tetroxide. Cells were then dehydrated with successive ethanol baths (30, 50 70, 90, 100 %) with increasing concentrations and finally embedded in the resin (Epon 812). Sections (40 nm thick and 3 mm long) were cut with the UC7RT ultramicrotome (Leica Microsystems GmbH), deposited onto TEM copper grids and stained with uranyless solution for 10 min and Reynolds lead citrate 3% for 3 min. Electron micrographs were recorded with a Tecnai G2 BioTWIN (FEI Company, Eindhoven, Netherlands) equipped with a CCD camera (Megaview III, Olympus Soft imaging Solutions GmbH, Münster, Germany) with an accelerating voltage of 100 kV. The sizes of magnetosomes were measured from TEM images using the ImageJ software (v1.48).

High-resolution transmission electron microscopes (HRTEM) and X-ray energy-dispersive spectrometry (XEDS). HRTEM was performed on cells directly deposited onto TEM copper grids coated with a carbon film. HRTEM and z-contrast imaging in the high-angle annular dark field (STEM-HAADF) mode, and elemental mapping by XEDS were carried out using a JEOL 2100 F microscope operating at

200 kV. This machine was equipped with a Schottky emission gun and an ultra-high-resolution pole piece. HRTEM images were obtained with a Gatan US 4000 charge-coupled-device (CCD) camera.

Cryo soft X-ray tomography (cryo-SXT). Imaging was conducted at ALBA synchrotron using cryo transmission X-ray microscopy at Mistral beamline (Barcelona, Spain) (63) under the awarded proposals 2018022677 and 2019023346. Using a similar approach to that described above, MHB samples were magnetically concentrated on the wall of an environmental sample bottle and then extracted by micropipette. 5 µL of the magnetically concentrated MHB extract along with 1 µL of 100 nm Au nanoparticles (BBI Solutions concentrated 5X) were added to a poly-l-lysine coated transmission electron microscopy grids (Quantafoil R2/2 holey carbon, gold). Gold nanoparticles of 100 nm deposited on the grid served as fiducial markers for projection alignment prior to tomographic reconstruction. The grid was incubated horizontally for 1-2 min to allow deposition of MHB on the grid. The grid was then vertically loaded into a Leica EM GP plunge freezer at 95 % humidity, blotted from the back of the grid with filter paper (3 s blotting time) and then quickly dropped into a liquid ethane container (-180 ºC) cooled by liquid nitrogen. Vitrified cells were kept under cryogenic conditions until being transferred to the MISTRAL beamline cryo chamber for measurement. Tomograms of two MHB were collected.

A tilt series of projections from -65 ° to +65 ° was collected every 1 ° with an incident X-ray energy of 520 eV. Exposure time varied from 1-2 s for each projection (2 s at higher angles). The sample was imaged at 0 ° before and after collecting the tilt series to ensure there was no significant beam damage at the achievable resolution. A 40 nm Fresnel zone plate was used with an effective pixel size of 12 nm. The projections were normalized with the incoming flux and deconvolved with the measured point spread function (PSF) of the optical system (64). Alignment of projections was done with Etomo using Au fiducials of 100 nm. Tomographic reconstruction and SIRT deconvolution were performed using IMOD. Volume segmentation and visualization of tomograms was conducted using Microscopy Image Browser (65) and Amira (FEI, USA) (66). Although this approach conserves the organization of MHB cells in their native-state configuration, partial detachment of ectosymbionts was observed. However, the majority of bacteria and their overall organization at the surface of their host were maintained.

Scanning transmission X-ray microscopy (STXM) and X-ray magnetic circular dichroism (XMCD). Magnetotactic holobionts were magnetically concentrated using a low intensity magnet (~10 mT) for a maximum time of 30 min to avoid remagnetization or any magnetic disturbance/interference with magnetosomes. Cells were then transferred onto a light microscopy slide and magnetically transferred in a clean drop of filtered environmental seawater. Cells aggregated at the edge of the filtered drop were then micromanipulated with an InjectMan® NI2 micromanipulator and a CellTram® vario, hydraulic, manual

microinjector from Eppendorf mounted to a Leica DM IL LED microscope and further transferred in a drop of fixative buffer containing 2.5 % (w/v) glutaraldehyde in sodium cacodylate buffer (0.1 M, pH 7.4) prepared in filtered environmental seawater. Fixation occurred for only 10 seconds at room temperature before the transfer of the cells, using the micromanipulator, onto a TEM copper grid coated with a carbon film. A quick fixation was sufficient to conserve the ultrastructure of the holobiont and allow observation of the biont's magnetosomes in the TEM. After their preparation, TEM grids were observed with STXM without previous TEM analysis to avoid magnetic disturbance.

STXM-XMCD measurements were performed at HERMES, the soft X-ray spectromicroscopy beamline at SOLEIL synchrotron (St. Aubin, France) (67, 68). A 25 nm Fresnel zone plate was employed with measurements conducted under vacuum conditions at room temperature. Most STXM maps of MHB were collected at 710 eV (at the Fe L_3-edge). Circularly polarized right (CPR) and left (CPL) light was used without applied magnetic field to conserve the native-state magnetic moment of magnetosomes. To retrieve an XMCD signal without applied fields, the sample was tilted 30 ° relative to the focal plane to measure the intrinsic magnetic dipole moments of magnetosomes (38). XMCD maps were then generated from the difference of OD-converted CPR and CPL images at 708.8 eV, the energy at which the strongest XMCD signal was found. Other energies corresponded to 709.9 and 711.0 eV. Axis2000 and IgorPro software were used to perform image work-up, analyses and create XMCD maps. XMCD maps were obtained for at least five MEB of each of the three MHB measured.

Micromagnetic simulations and calculations. To determine the decay of the stray field from a straight chain of 25 magnetosomes, we use a non-interacting point dipole approximation. Each point dipole is taken to represent the center of a rhomboidal dodecahedron magnetosome with mid-sphere diameter of 60 nm (volume of 7.0×10^{-23} m^3), which, with a magnetite saturation magnetization of 4.8×10^5 $A \cdot m^{-1}$, equates to a uniformly magnetized magnetosome moment of 3.36×10^{-17} $A \cdot m^2$ (total chain moment of 8.40×10^{-16} $A \cdot m^2$; 0.84 $fA \cdot m^2$). The magnetosome neighbor-to-neighbor edge separation is taken to be 10 nm. The net stray field is calculated as the sum of 25 magnetosome dipole fields at given distances parallel and perpendicular to the chain axis (Fig. S7).

Micromagnetic models were used to determine the effect of curved chains around the host cell. Magnetosome size, shape, and neighbor-to-neighbor edge separation are the same as described above. The magnetosome chains were arranged in an arc defined by a circle of a specified radius, while maintaining the face centered neighbor-to-neighbor edge separation of 10 nm. Mesh inputs were generated using Trelis v17.1. The micromagnetic calculations were performed using MERRILL v1.6.4 (37). An example of a micromagnetic solution is shown in Fig. S8.

For a population of cells, the average alignment, <cosθ>, is dependent on the balance of magnetic energy rotating the cell towards the magnetic field and thermal energy of randomizing Brownian rotation. This can be expressed as:

$$\langle \cos\theta \rangle = L\left(\frac{mB}{k_B T}\right)$$

where m is the net moment of each cell, B is the magnetic field intensity, T is the temperature, k_B is the Boltzmann constant, and $L(x) = \coth x - {}^{1}/_{x}$, is the Langevin function. A magnetotactic advantage will be conferred to a population of cells if there is a net average bias of alignment of cells towards the magnetic field direction where <cosθ> ≥ 0.5. Over the past 10,000 years in the Mediterranean region, the field strength is consistently above 30 μT, which, at 20 °C, equates to a minimum moment per cell of 0.24 fA·m^2. For an extremely weak field of 3 μT, a minimum moment per cell of 2.4 fA·m^2 is required to overcome Brownian motion and can be achieved with as few as two chains of magnetosomes (Fig. S8).

Acknowledgements

This work was supported by a grant from the CNRS – mission pour les initiatives transverses et interdisciplinaires (MITI), adaptation du vivant à son environnement, projet *SymbioAdapt* and a project from the French National Research Agency (ANR SymbioMagnet-21-CE02-0034-01). Romain Bolzoni PhD contract was supported by the CNRS – MITI. D.M.C. acknowledges research funding through a European Union Marie-Skłodowska Curie Action International Fellowship (MSCA-IF Project 797431: BioNanoMagnets). D.M.C. and D.F. acknowledge awarded ALBA synchrotron beamtimes (Proposals 2018022677 and 2019023346), Mistral beamline staff for assistance in cryo-SXT experiments and CALIPSO funding for Proposal 2019023346. We acknowledge Soleil Synchrotron for beamtime awarded (Proposal 20191124) for experiments on the Hermes beamline (STXM-XMCD). W.W. would like to acknowledge support from the Natural Environmental Research Council (NERC) through grants NE/V001233/1 and NE/S011978/1. We thank Suri for his help in ultrathin-sections preparation. We thank Jean-Michel Guigner for managing the TEM facility at IMPMC. G.A.P. is funded by a Natural Environment Research Council Independent Research Fellowship (NE/P017266/1).

References

1. J.-B. Raina, *et al.*, Symbiosis in the microbial world: from ecology to genome evolution. *Biol. Open* **7**, bio032524 (2018).

2. L. Margulis, R. Fester, *Symbiosis as a Source of Evolutionary Innovation: Speciation and Morphogenesis* (MIT Press, 1991).

3. P. Lopez-Garcia, D. Moreira, The Syntrophy hypothesis for the origin of eukaryotes revisited. *Nat. Microbiol.* **5**, 655–667 (2020).

4. P. López-García, L. Eme, D. Moreira, Symbiosis in eukaryotic evolution. *J. Theor. Biol.* **434**, 20–33 (2017).

5. P. Engel, N. A. Moran, The gut microbiota of insects - diversity in structure and function. *Fems Microbiol. Rev.* **37**, 699–735 (2013).

6. P. Vandenkoornhuyse, A. Quaiser, M. Duhamel, A. Le Van, A. Dufresne, The importance of the microbiome of the plant holobiont. *New Phytol.* **206**, 1196–1206 (2015).

7. T. Woyke, *et al.*, Symbiosis insights through metagenomic analysis of a microbial consortium. *Nature* **443**, 950–955 (2006).

8. C. E. Harper, C. J. Hernandez, Cell biomechanics and mechanobiology in bacteria: Challenges and opportunities. *APL Bioeng.* **4**, 021501 (2020).

9. J. Decelle, *et al.*, Subcellular architecture and metabolic connection in the planktonic photosymbiosis between Collodaria (radiolarians) and their microalgae. *Environ. Microbiol.* **23**, 6569–6586 (2021).

10. J.-C. Simon, J. R. Marchesi, C. Mougel, M.-A. Selosse, Host-microbiota interactions: from holobiont theory to analysis. *Microbiome* **7**, 5 (2019).

11. D. Faure, J.-C. Simon, T. Heulin, Holobiont: a conceptual framework to explore the eco-evolutionary and functional implications of host-microbiota interactions in all ecosystems. *New Phytol.* **218**, 1321–1324 (2018).

12. P. López-García, D. Moreira, Open questions on the origin of eukaryotes. *Trends Ecol. Evol.* **30**, 697–708 (2015).

13. M. Müller, *et al.*, Biochemistry and evolution of anaerobic energy metabolism in eukaryotes. *Microbiol. Mol. Biol. Rev. MMBR* **76**, 444–495 (2012).

14. E. Hamann, *et al.*, Environmental Breviatea harbor mutualistic Arcobacter epibionts. *Nature* **534**, 254–258 (2016).

15. T. Vicsek, A. Zafeiris, Collective motion. *Phys. Rep.* **517**, 71–140 (2012).

16. A. M. Wier, *et al.*, Spirochete attachment ultrastructure: Implications for the origin and evolution of cilia. *Biol. Bull.* **218**, 25–35 (2010).

17. C. L. Monteil, *et al.*, A symbiotic origin of magnetoreception in unicellular eukaryotes. *Nat. Microbiol.* **4**, 1088–1095 (2019).

18. D. A. Bazylinski, R. B. Frankel, Magnetosome formation in prokaryotes. *Nat. Rev. Microbiol.* **2**, 217–230 (2004).

19. C. T. Lefèvre, *et al.*, Diversity of magneto-aerotactic behaviors and oxygen sensing mechanisms in cultured magnetotactic bacteria. *Biophys. J.* **107**, 527–538 (2014).

20. X. Mao, R. Egli, X. Liu, L. Zhao, Magnetotactic advantage in stable sediment by long-term observations of magnetotactic bacteria in Earth's field, zero field and alternating field. *PloS One* **17**, e0263593 (2022).

21. X.-X. Qian, *et al.*, Juxtaposed membranes underpin cellular adhesion and display unilateral cell division of multicellular magnetotactic prokaryotes. *Environ. Microbiol.* **22**, 1481–1494 (2020).

22. D. Pfeiffer, *et al.*, A bacterial cytolinker couples positioning of magnetic organelles to cell shape control. *Proc. Natl. Acad. Sci. U. S. A.* **117**, 32086–32097 (2020).

23. M. Toro-Nahuelpan, *et al.*, MamY is a membrane-bound protein that aligns magnetosomes and the motility axis of helical magnetotactic bacteria. *Nat. Microbiol.* **4**, 1978–1989 (2019).

24. C. T. Lefèvre, M. Bennet, S. Klumpp, D. Faivre, Positioning the Flagellum at the Center of a Dividing Cell To Combine Bacterial Division with Magnetic Polarity. *mBio* **6**, e02286 (2015).

25. M. Toro-Nahuelpan, *et al.*, Segregation of prokaryotic magnetosomes organelles is driven by treadmilling of a dynamic actin-like MamK filament. *BMC Biol.* **14**, 88 (2016).

26. M. L. Ginger, N. Portman, P. G. McKean, Swimming with protists: perception, motility and flagellum assembly. *Nat. Rev. Microbiol.* **6**, 838–850 (2008).

27. D. Esquivel, H. Debarros, M. Farina, P. Aragao, J. Danon, Magnetotactic Microorganisms in the Rio-De-Janeiro Region. *Biol. Cell* **47**, 227–233 (1983).

28. M. Perantoni, *et al.*, Magnetic properties of the microorganism Candidatus Magnetoglobus multicellularis. *Naturwissenschaften* **96**, 685–690 (2009).

29. F. F. T. de Araujo, M. A. Pires, R. B. Frankel, C. E. M. Bicudo, Magnetite and Magnetotaxis in Algae. *Biophys. J.* **50**, 375–378 (1986).

30. P. Leão, *et al.*, Magnetosome magnetite biomineralization in a flagellated protist: evidence for an early evolutionary origin for magnetoreception in eukaryotes? *Environ. Microbiol.* **22**, 1495–1506 (2019).

31. M. P. Pichel, T. A. G. Hageman, I. S. M. Khalil, A. Manz, L. Abelmann, Magnetic response of Magnetospirillum gryphiswaldense observed inside a microfluidic channel. *J. Magn. Magn. Mater.* **460**, 340–353 (2018).

32. C. Zahn, *et al.*, Measurement of the magnetic moment of single Magnetospirillum gryphiswaldense cells by magnetic tweezers. *Sci. Rep.* **7**, 1–14 (2017).

33. R. Nadkarni, S. Barkley, C. Fradin, A comparison of methods to measure the magnetic moment of magnetotactic bacteria through analysis of their trajectories in external magnetic fields. *PLoS ONE* **8**, e82064 (2013).

34. R. E. Dunin-Borkowski, *et al.*, Magnetic microstructure of magnetotactic bacteria by electron holography. *Science* **282**, 1868–1870 (1998).

35. F. Abreu, *et al.*, Cell adhesion, multicellular morphology, and magnetosome distribution in the multicellular magnetotactic prokaryote Candidatus Magnetoglobus multicellularis. *Microsc. Microanal. Off. J. Microsc. Soc. Am. Microbeam Anal. Soc. Microsc. Soc. Can.* **3**, 1–9 (2013).

36. P. Leão, *et al.*, Ultrastructure of ellipsoidal magnetotactic multicellular prokaryotes depicts their complex assemblage and cellular polarity in the context of magnetotaxis. *Environ. Microbiol.* **19**, 2151–2163 (2017).

37. P. O. Conbhui, *et al.*, MERRILL: Micromagnetic Earth Related Robust Interpreted Language Laboratory. *Geochem. Geophys. Geosystems* **19**, 1080–1106 (2018).

38. L. Le Nagard, *et al.*, Magnetite magnetosome biomineralization in Magnetospirillum magneticum strain AMB-1: A time course study. *Chem. Geol.* **530**, 119348 (2019).

39. F. C. Meldrum, S. Mann, B. R. Heywood, R. B. Frankel, D. A. Bazylinski, Electron-microscopy study of magnetosomes in a cultured coccoid magnetotactic bacterium. *Proc. R. Soc. Lond. Ser. B-Biol. Sci.* **251**, 231–236 (1993).

40. F. C. Meldrum, S. Mann, B. R. Heywood, R. B. Frankel, D. A. Bazylinski, Electron-microscopy study of magnetosomes in 2 cultured vibrioid magnetotactic bacteria. *Proc. R. Soc. Lond. Ser. B-Biol. Sci.* **251**, 237–242 (1993).

41. M. Pósfai, C. T. Lefèvre, D. Trubitsyn, D. A. Bazylinski, R. B. Frankel, Phylogenetic significance of composition and crystal morphology of magnetosome minerals. *Front. Microbiol.* **4**, 344 (2013).

42. M. Winklhofer, L. G. Abraçado, A. F. Davila, C. N. Keim, H. G. P. Lins de Barros, Magnetic optimization in a multicellular magnetotactic organism. *Biophys. J.* **92**, 661–670 (2007).

43. C. T. Lefèvre, *et al.*, Monophyletic origin of magnetotaxis and the first magnetosomes. *Environ. Microbiol.* **15**, 2267–2274 (2013).

44. E. C. T. Descamps, J.-B. Abbé, D. Pignol, C. T. Lefèvre, "Controlled Biomineralization of Magnetite in Bacteria" in *Iron Oxides*, D. Faivre, Ed. (Wiley-VCH Verlag GmbH & Co. KGaA, 2016), pp. 99–116.

45. R. B. Frankel, R. P. Blakemore, Navigational compass in magnetic bacteria. *J. Magn. Magn. Mater.* **15–8**, 1562–1564 (1980).

46. D. M. S. Esquivel, H. G. P. Lins De Barros, Motion of Magnetotactic Microorganisms. *J. Exp. Biol.* **121**, 153–163 (1986).

47. N. Petersen, D. G. Weiss, H. Vali, "Magnetic bacteria in lake sediments" in *Geomagnetism and Palaeomagnetism*, NATO ASI Series., F. J. Lowes, *et al.*, Eds. (Springer Netherlands, 1989), pp. 231–241.

48. Y. Pan, *et al.*, Reduced efficiency of magnetotaxis in magnetotactic coccoid bacteria in higher than geomagnetic fields. *Biophys. J.* **97**, 986–991 (2009).

49. E. Wajnberg, L. Desouza, H. Debarros, D. Esquivel, A Study of Magnetic-Properties of Magnetotactic Bacteria. *Biophys. J.* **50**, 451–455 (1986).

50. S. S. Kalirai, D. A. Bazylinski, A. P. Hitchcock, Anomalous magnetic orientations of magnetosome chains in a magnetotactic bacterium: Magnetovibrio blakemorei strain MV-1. *PloS One* **8**, e53368 (2013).

51. E. F. DeLong, R. B. Frankel, D. A. Bazylinski, Multiple evolutionary origins of magnetotaxis in bacteria. *Science* **259**, 803–806 (1993).

52. W. Lin, *et al.*, Origin of microbial biomineralization and magnetotaxis during the Archean. *Proc. Natl. Acad. Sci. U. S. A.* **114**, 2171–2176 (2017).

53. J. M. Byrne, *et al.*, Redox cycling of Fe(II) and Fe(III) in magnetite by Fe-metabolizing bacteria. *Science* **347**, 1473–1476 (2015).

54. V. P. Edgcomb, *et al.*, Identity of epibiotic bacteria on symbiontid euglenozoans in O2-depleted marine sediments: evidence for symbiont and host co-evolution. *ISME J.* **5**, 231–243 (2011).

55. F. F. Guo, *et al.*, Magnetosomes eliminate intracellular reactive oxygen species in Magnetospirillum gryphiswaldense MSR-1. *Environ. Microbiol.* **14**, 1722–1729 (2012).

56. K. Li, *et al.*, Magnetosomes extracted from Magnetospirillum magneticum strain AMB-1 showed enhanced peroxidase-like activity under visible-light irradiation. *Enzyme Microb. Technol.* **72**, 72–78 (2015).

57. T. Fenchel, B. Finlay, Oxygen and the spatial structure of microbial communities. *Biol. Rev. Camb. Philos. Soc.* **83**, 553–569 (2008).

58. D. Schüler, E. Baeuerlein, Dynamics of iron uptake and Fe3O4 biomineralization during aerobic and microaerobic growth of Magnetospirillum gryphiswaldense. *J. Bacteriol.* **180**, 159–162 (1998).

59. R. B. Frankel, D. A. Bazylinski, M. S. Johnson, B. L. Taylor, Magneto-aerotaxis in marine coccoid bacteria. *Biophys. J.* **73**, 994–1000 (1997).

60. N. Philippe, L.-F. Wu, An MCP-like protein interacts with the MamK cytoskeleton and is involved in magnetotaxis in Magnetospirillum magneticum AMB-1. *J. Mol. Biol.* **400**, 309–322 (2010).

61. D. Schüler, The biomineralization of magnetosomes in Magnetospirillum gryphiswaldense. *Int. Microbiol. Off. J. Span. Soc. Microbiol.* **5**, 209–214 (2002).

62. M. Bennet, *et al.*, Influence of Magnetic Fields on Magneto-Aerotaxis. *PLoS ONE* **9**, e101150 (2014).

63. A. Sorrentino, *et al.*, MISTRAL: a transmission soft X-ray microscopy beamline for cryo nano-tomography of biological samples and magnetic domains imaging. *J. Synchrotron Radiat.* **22**, 1112–1117 (2015).

64. J. Otón, *et al.*, Characterization of transfer function, resolution and depth of field of a soft X-ray microscope applied to tomography enhancement by Wiener deconvolution. *Biomed. Opt. Express* **7**, 5092–5103 (2016).

65. I. Belevich, M. Joensuu, D. Kumar, H. Vihinen, E. Jokitalo, Microscopy Image Browser: A Platform for Segmentation and Analysis of Multidimensional Datasets. *PLOS Biol.* **14**, e1002340 (2016).

66. D. Stalling, M. Westerhoff, H.-C. Hege, "38 - amira: A Highly Interactive System for Visual Data Analysis" in *Visualization Handbook*, C. D. Hansen, C. R. Johnson, Eds. (Butterworth-Heinemann, 2005), pp. 749–767.

67. R. Belkhou, *et al.*, HERMES: a soft X-ray beamline dedicated to X-ray microscopy. *J. Synchrotron Radiat.* **22**, 968–979 (2015).

68. S. Swaraj, *et al.*, Performance of the HERMES beamline at the carbon K-edge. *J. Phys. Conf. Ser.* **849**, 012046 (2017).

722 **Figures legend**

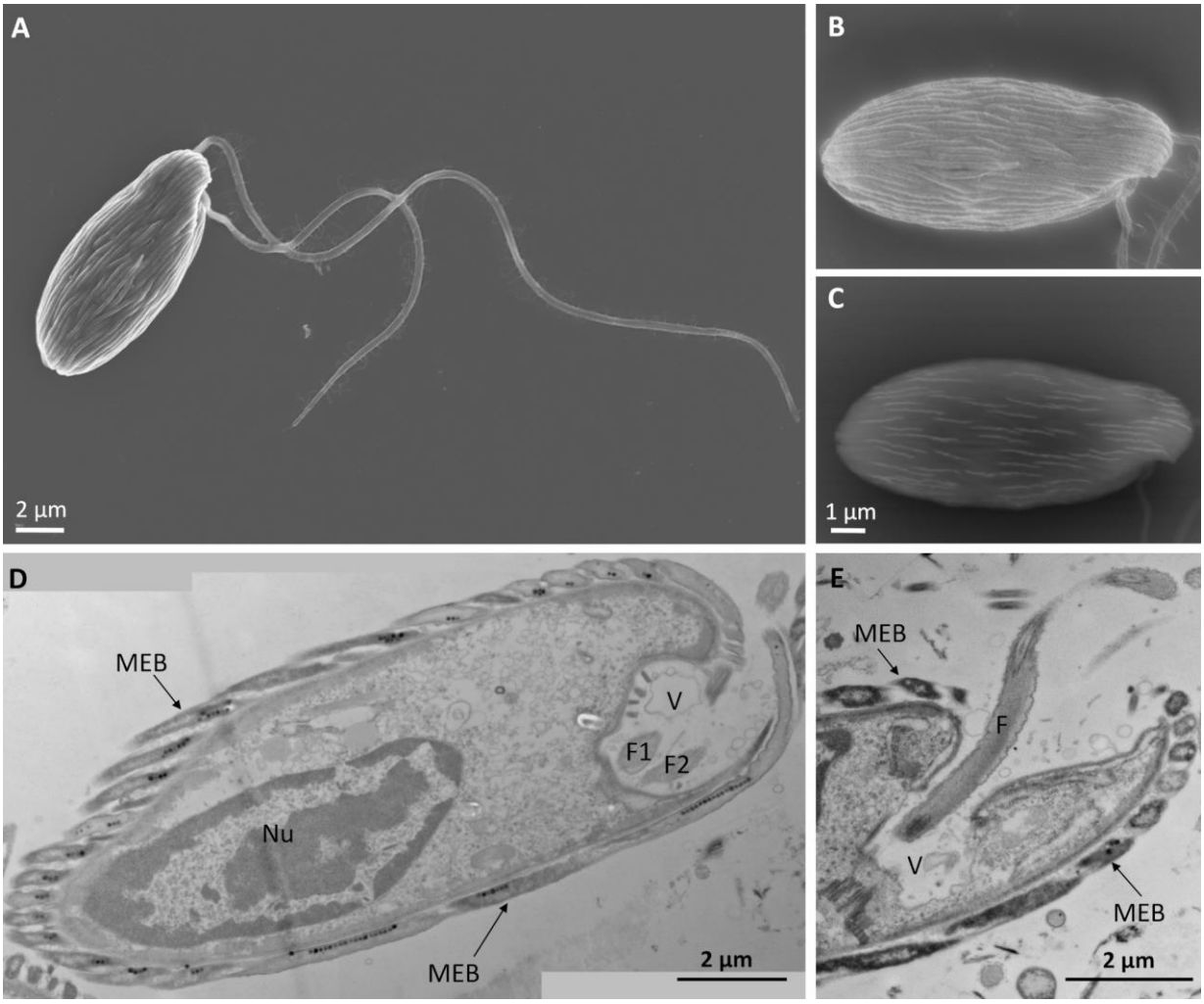

723

724 **Fig. 1. Observation of the motility apparatus of MHBs isolated from Carry-le-Rouet, France.** (*A-C*)
725 SEM images of cells prepared using a critical-point drying approach showing (*A*) a whole MHB, (*B*) a
726 higher magnification of the same holobiont observed at 2 kV showing the surface of the holobiont, and (*C*)
727 the same as in (B) but observed at 10 kV using the backscattered mode showing the magnetosome chains
728 inside the ectosymbiotic bacteria. (*D*) Stitched TEM images of longitudinal ultrathin sections of a MHB
729 showing the vestibulum on the front of the protistan cells and the two flagella and (*E*) TEM image showing
730 one flagellum emerging from this cavity. Nu: nucleus; MEB: magnetic ectosymbiotic bacteria; F: flagella;
731 V: vestibulum.

732

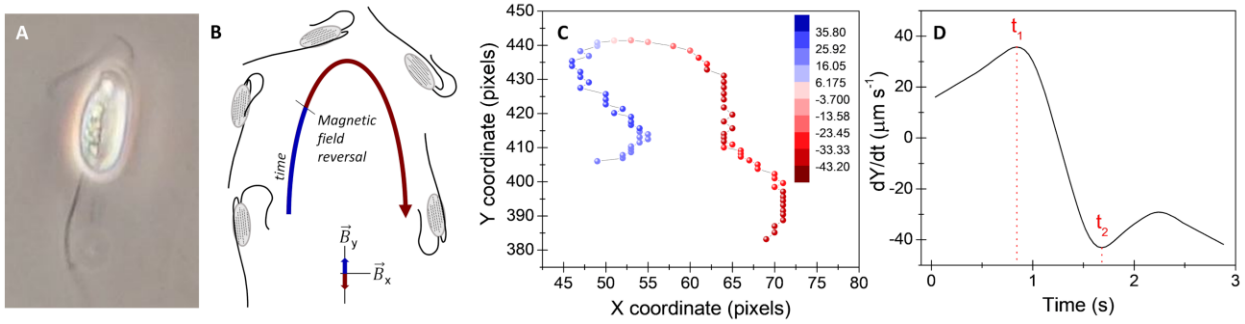

733

734 **Fig. 2. Observation of the magnetic response of MHBs isolated from Carry-le-Rouet, France.** (*A*)
735 Optical microscopy image of a swimming MHB showing the position of the flagella. (*B*) Schematic of U-
736 turn trajectory measurements during magnetic field reversal. (*C*) The trajectory plot of a U-turn at 3.5 mT
737 magnetic field switching. The instantaneous velocity (µm·s^{-1}) is represented in color indicating the MHB
738 motility direction where the blue color indicates upwards motion and red color the downward displacement.
739 (*D*) Time difference subtracted from first derivate peaks (t_1 and t_2) of the Y trajectory to yield τ_{Uturn}.

740

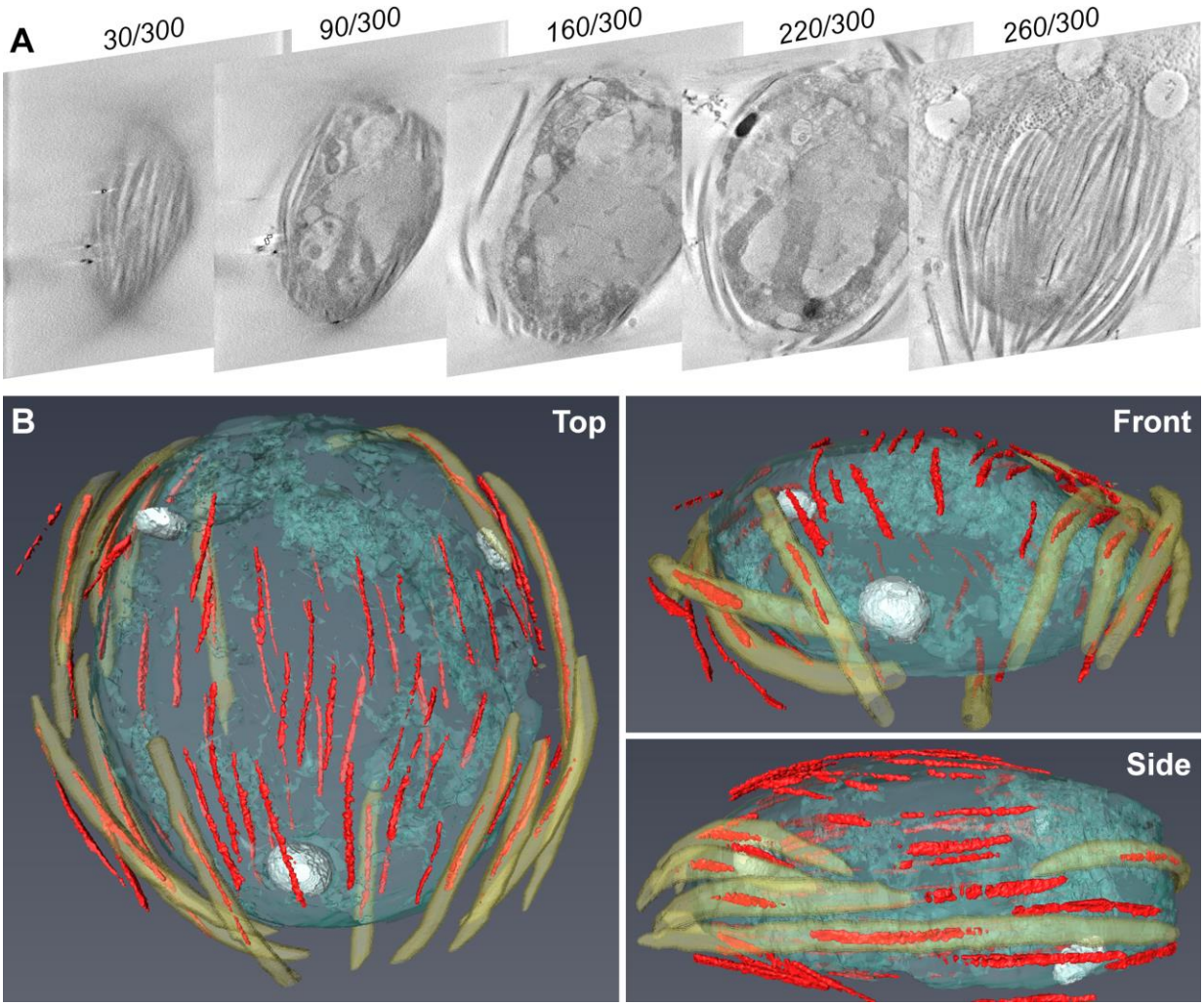

741

742 **Fig. 3. 3-D reconstruction of vitrified MHB using cryo soft X-ray tomography (cryo-SXT).** (*A*) Virtual
743 slices of X-ray tomography reconstruction through the Z-direction from top to bottom of MHB (see Movie
744 S2). (*B*) Volume reconstruction of magnetosome chains (red), ectosymbiotic bacteria membrane (yellow),
745 the protistan host (cyan) and dense intracellular granules (white) from different viewpoints.

746

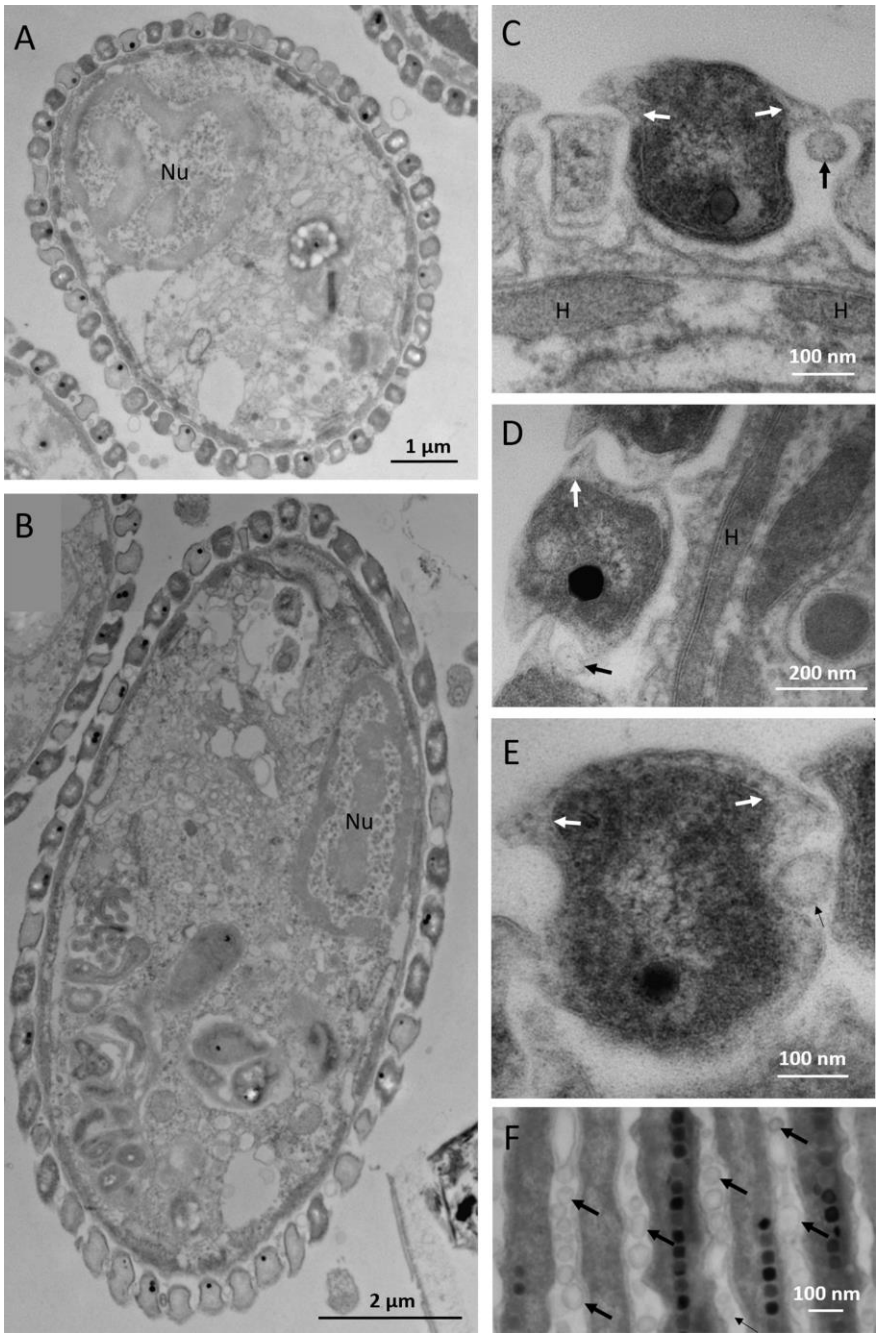

Fig. 4. Organization and attachment of ectosymbiotic bacteria at the surface of their host. Transmission electron microscope images in bright field mode of ultrathin sections of MHB showing (*A,B*) the presence of only one layer of bacteria at the surface of their host, (*C*) the presence of bacteria in channels formed at the surface of their host, (*C,D*) the proximity of ectosymbionts with hydrogenosomes, (*C-E,* white arrows) the wing-like structures that are outgrowths of bacterial external membrane, and (*C-F*, black arrows) the presence of vesicles between the bacteria. Nu: nucleus; H: hydrogenosomes. All are transverse sections except for *F*, which is longitudinal.

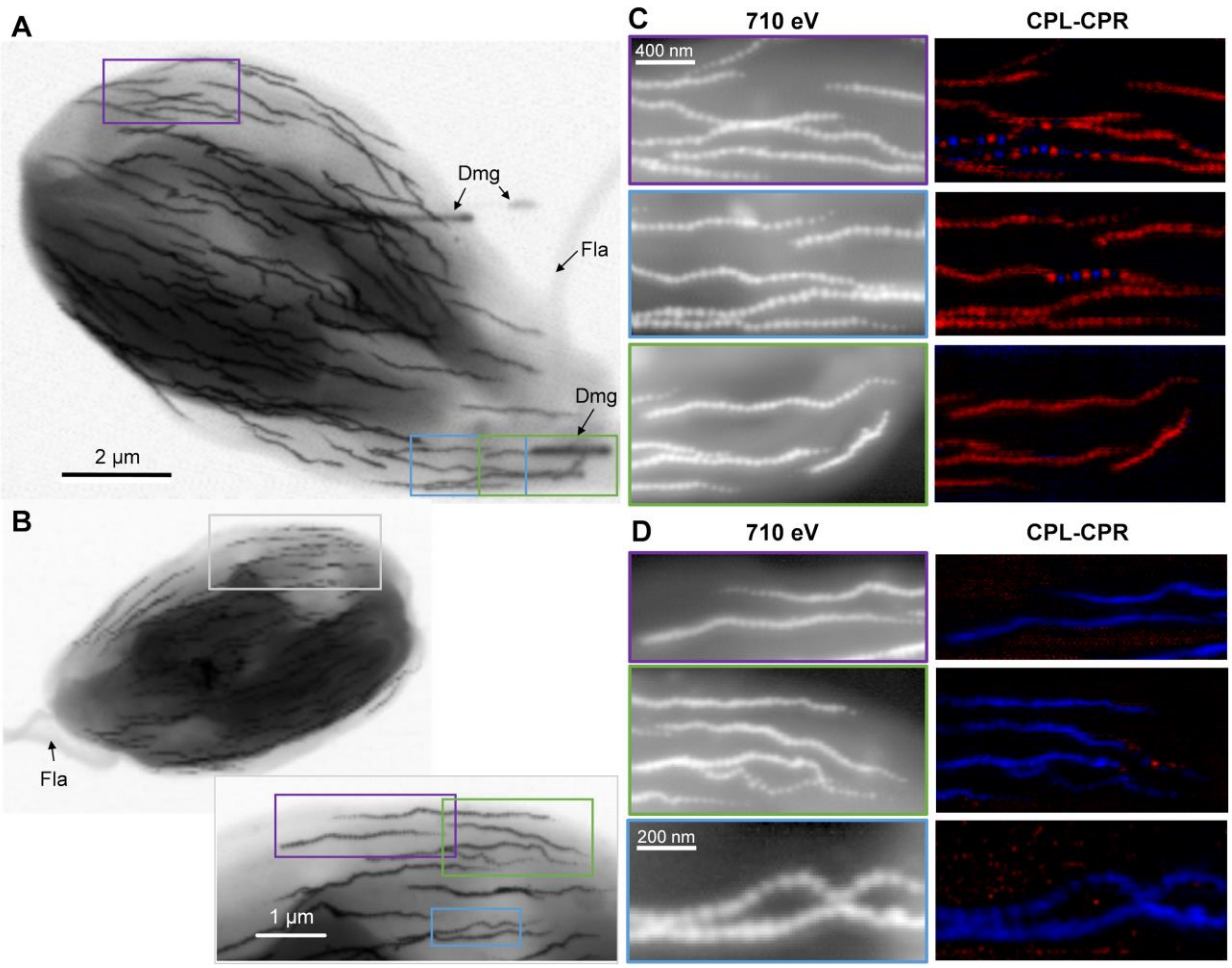

Fig. 5. Magnetic moment orientation of magnetosomes relative to the protistan flagella using soft X-ray scanning transmission X-ray microscopy (STXM) at the Fe L-edge and X-ray magnetic circular dichroism (XMCD) without applied magnetic fields. (*A*,*B*) STXM images at 710 eV of MHB deposited in opposite directions. Fla: flagella; Dmg: X-ray beam damage from previous scans. Colored frames indicate the regions further analyzed. (*C*,*D*) Optical density maps (left-side panels) and difference maps of circular polarization left (CPL) and circular polarization right (CPR) at 708.8 eV (where maximum XMCD signal was found) (right-side panels).

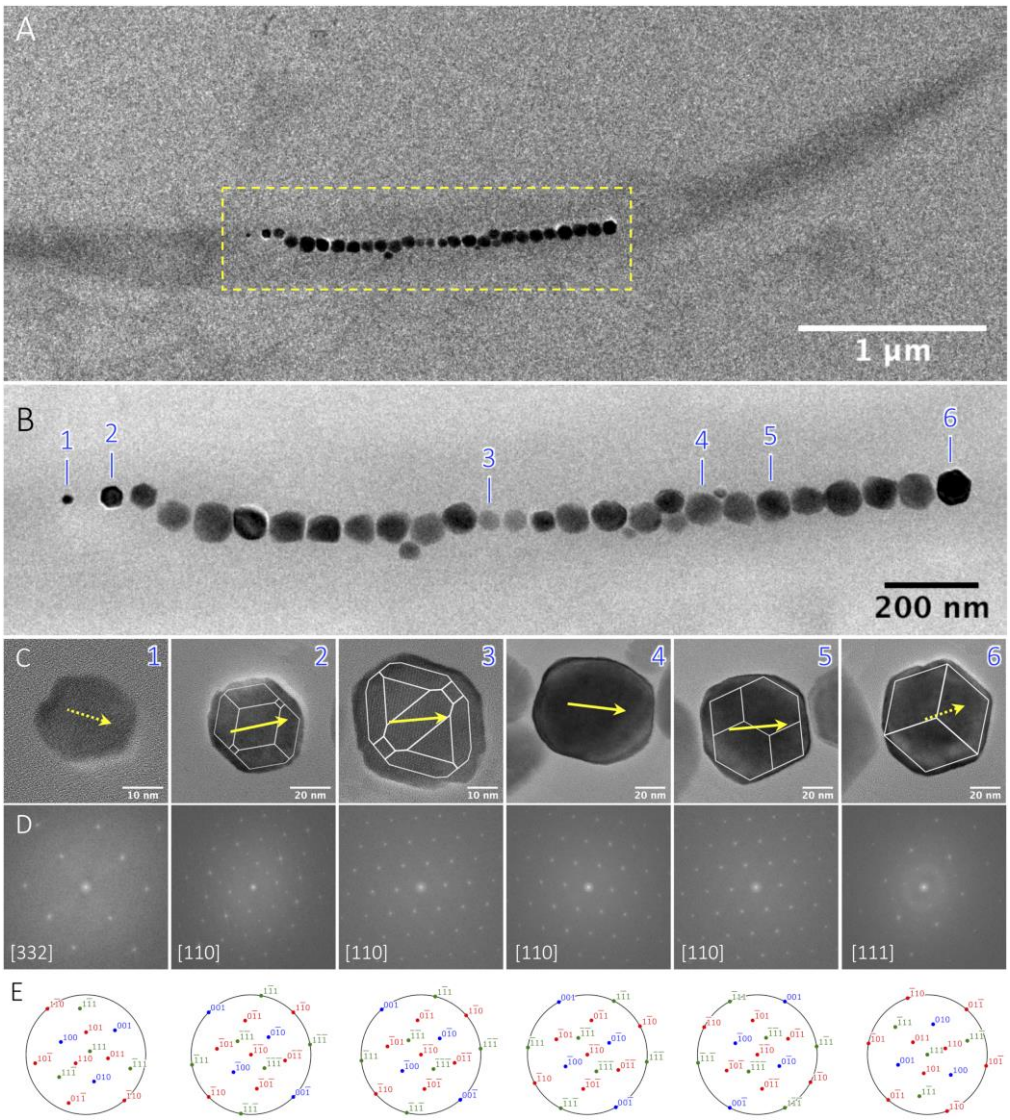

Fig. 6. Crystallography of the cuboctahedral/prismatic magnetite particles produced by a magnetic ectosymbiotic bacteria. (*A*) Transmission electron microscope bright-field (TEM-BF) image of a magnetic ectosymbiotic bacterium detached from its host and its single magnetosome chain (*B*). (*C*) High-resolution transmission electron microscopy (HR-TEM) images of the crystals annotated 1-6 in (*B*). Prismatic models drawn in white were superimposed on the image of these crystals with an acceptable match. Yellow arrows indicate the <111> direction: plain arrows correspond to in plane direction and dashed arrows are related to out-of-plane direction (for the latter, smaller arrow length corresponds to a higher out-of-plane angle). (*D*) FFT pattern of these HR-TEM indexed with the magnetite structure (spacegroup $Fm\bar{3}m$, a = 8.04 Å). (*E*) Stereographic projection oriented with respect to the orientation inferred from (*D*) using SingleCrystal software. The orientations of the models and the <111> directions were deduced from the stereographic projections.

Supporting Information for

Collective magnetotaxis of microbial holobionts is optimized by the three-dimensional organization and magnetic properties of ectosymbionts

Daniel M. Chevrier[1*], Amélie Juhin[2], Nicolas Menguy[2], Romain Bolzoni[1], Paul E. D. Soto-Rodriguez[1], Mila Kojadinovic-Sirinelli[1], Greig A. Paterson[3], Rachid Belkhou[4], Wyn Williams[5], Fériel Skouri-Panet[2], Artemis Kosta[6], Hugo Le Guenno[6], Eva Pereiro[7], Damien Faivre[1], Karim Benzerara[2], Caroline L. Monteil[1], Christopher T. Lefevre[1]*

*Corresponding author: Drs. Daniel Chevrier and Christopher T. Lefevre

Emails: daniel.chevrier@cea.fr and christopher.lefevre@cea.frThis PDF file includes:

Figs. S1 to S15

Movie S1. Light microscope movie of south-seeking magnetotactic holobionts sampled from Carry-le-Rouet, Mediterranean Sea, showing the motility of the consortium and the presence of two flagella emerging from the front of the protistan host.

Movie S2. Reconstructed tomogram of MHB from cryo-transmission X-ray microscopy (cTXM) imaging. Video depicts the volume contents by traversing the Z-direction.

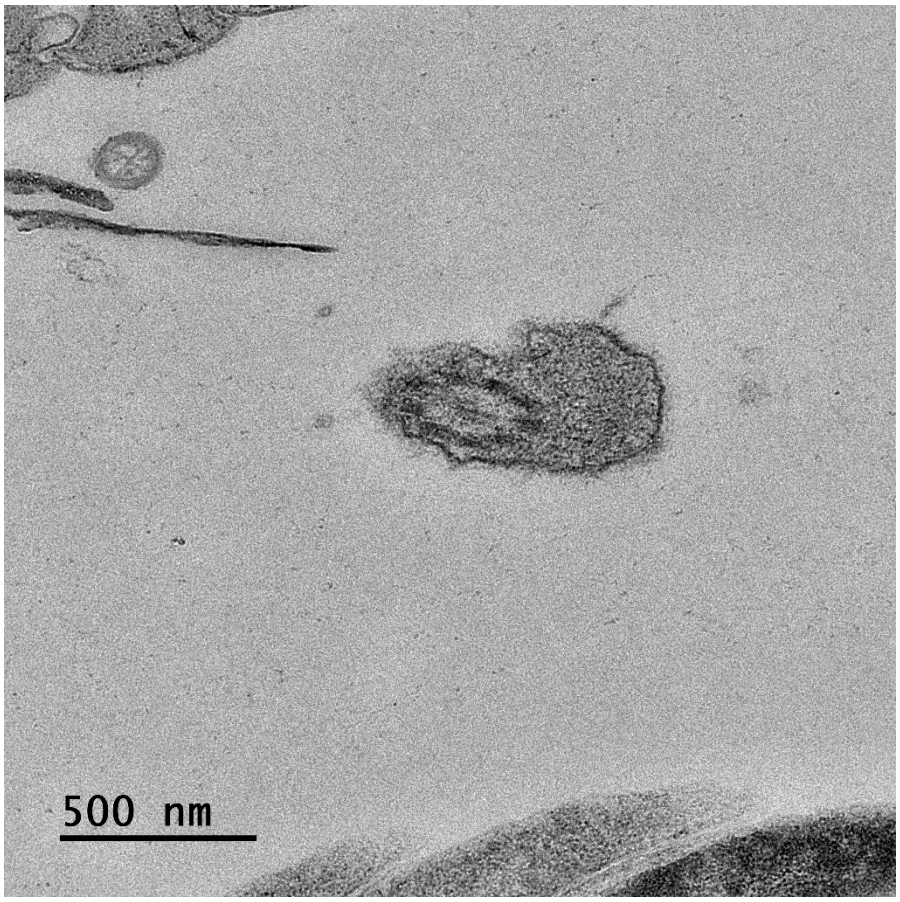

Fig. S1. Transmission electron microscope image of the transversal section of a flagellum of a protist carrying magnetic ectosymbiotic bacteria showing a canonical '9+2' microtubule axoneme structure.

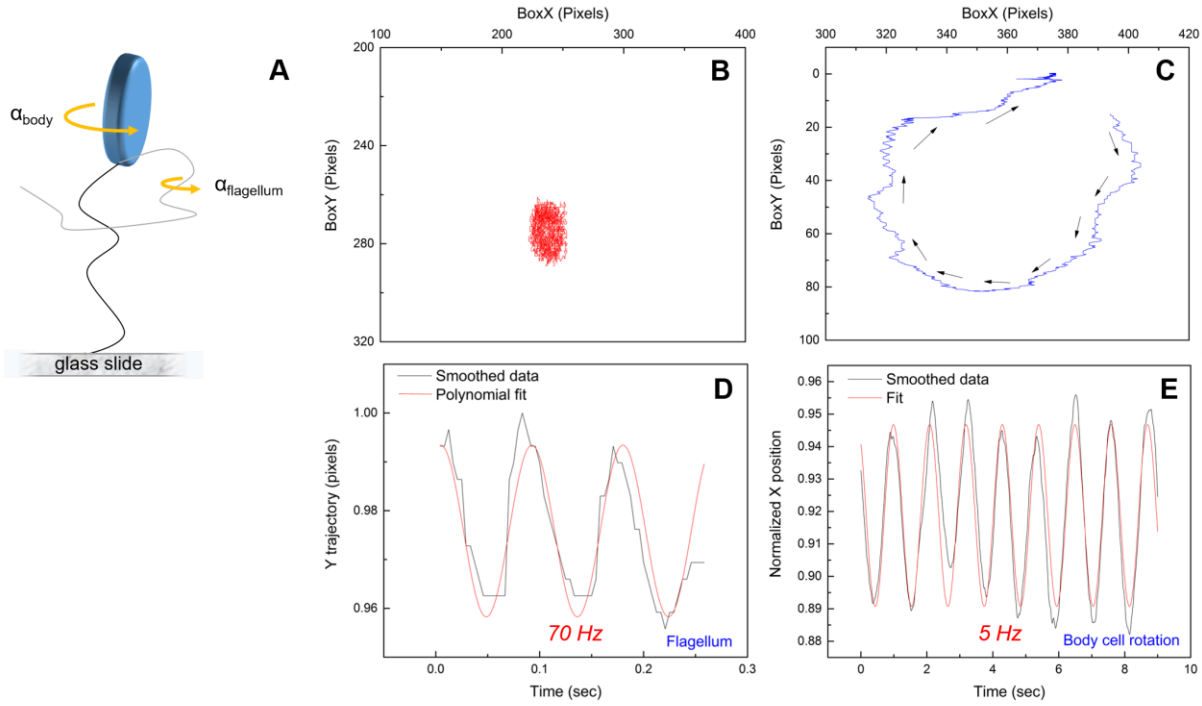

Fig. S2. Motility and magnetotactic behavior of MHBs. The swimming behavior of MHBs was investigated with live microscopy imaging within a framework of Helmholtz coils to control the local magnetic field strength around the specimen (Materials and Methods). (*A*) Model depiction of MHBs attached to the glass slide with one of their two flagella. A few instances of this provided an opportunity to estimate the rotational speed of the cell body (α_{body}) and flagellum ($\alpha_{flagellum}$). (*B*) An example of the tracked rotation of the cell body of attached MHB which allowed tracking of flagella rotation. (*C*) Example of 2D MHB trajectory when unbound and swimming close to glass slide surface, showing a circular motion with helicoidal motility where the cell body is rotating around its longitudinal axis. The mean cell velocity of freely-swimming MHBs in the bulk liquid (away from glass slide surface) was determined to be 107 $\mu m \cdot s^{-1}$, with a maximum of 155 $\mu m \cdot s^{-1}$ (n = 16). The rotational axis is parallel to the swimming trajectory during the entire swimming motion (see Movie S1). It was observed that a single in-plane rotation corresponds to one single body cell rotation, thus by tracking the in-plane circular motion the body rotation frequency can be extracted. By fitting extracted coordinate positions versus time Fig. 2B and 2C with $X=X_0+A\cos(\omega t)$, frequencies ($f=\omega/2\pi$) of (*D*) *ca.* 70 Hz for the flagellum and (*E*) *ca.* 5 Hz for the body cell are obtained for example.

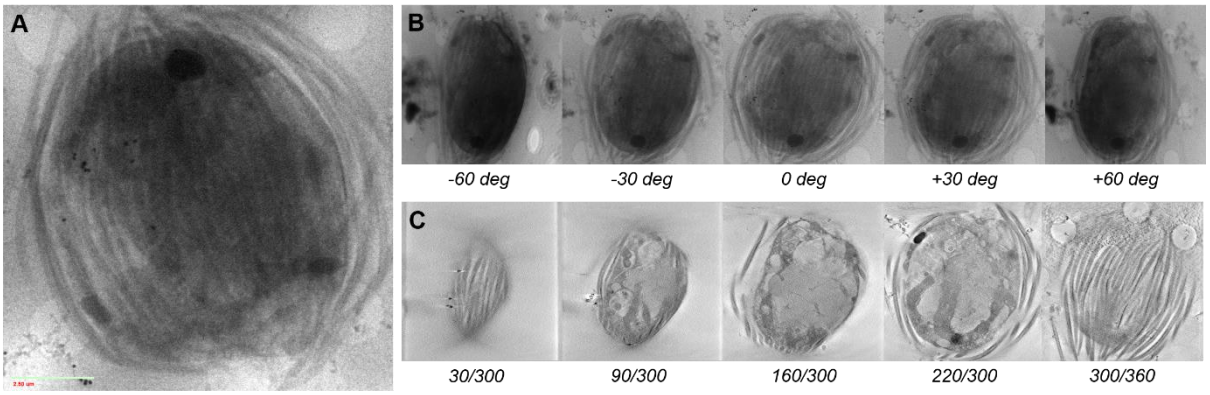

Fig. S3. Cryo soft X-ray tomography (cryo-SXT) of a MHB. (*A*) Raw X-ray image of MHB at 520 eV. (*B*) Tilt-series images and (*C*) reconstructed virtual slices (in Z-direction) of X-ray tomography data.

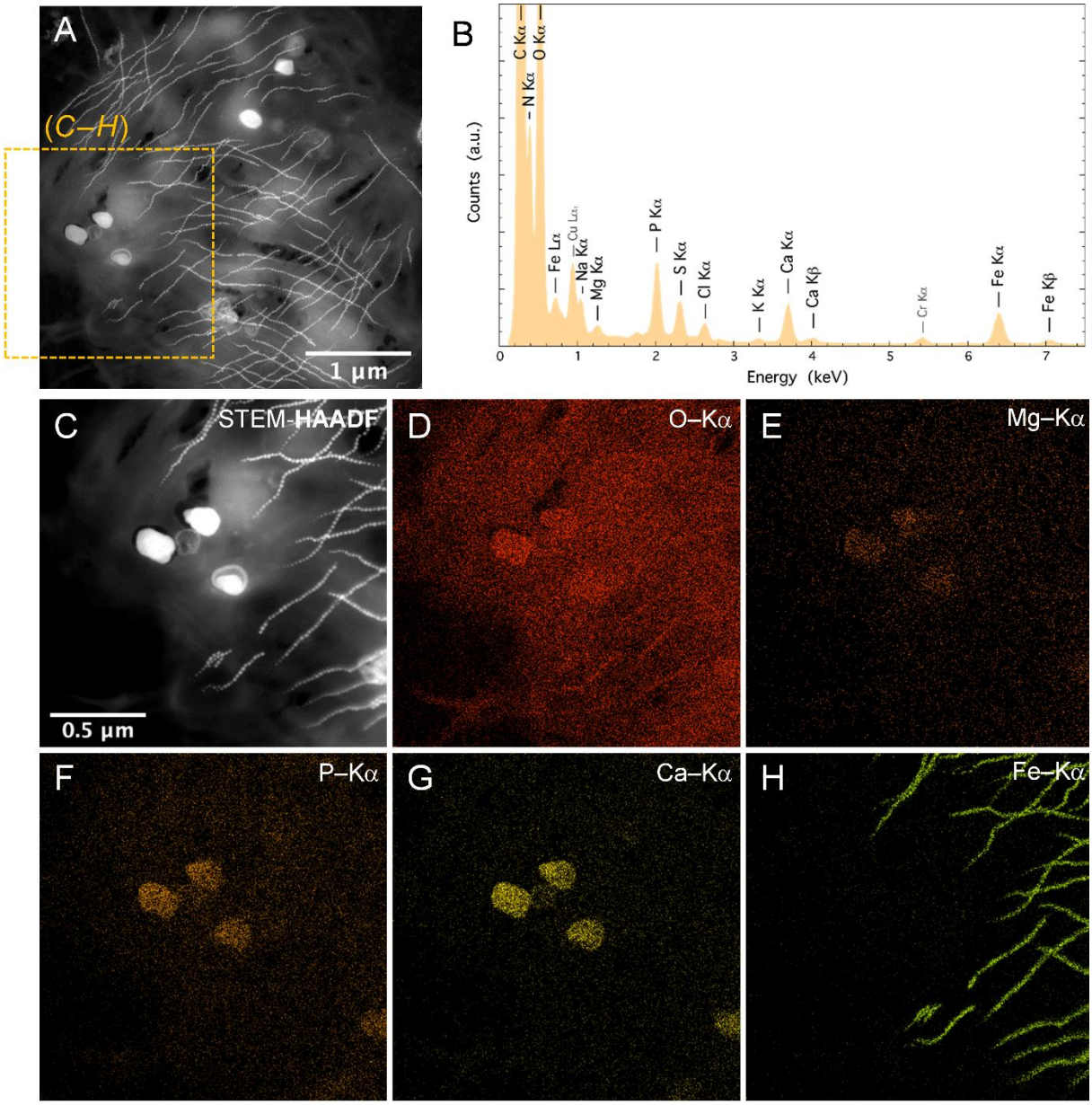

Fig. S4. Chemical identification of the inclusions found in MHBs. (*A*) STEM-HAADF image of an unfixed MHB. The dashed square corresponds to the region further analyzed. (*B*) XEDS elemental spectrum of an inclusion. (*C*) STEM-HAADF image of the region shown in (*A*) by a dashed square. XEDS elemental mapping of oxygen (*D*), magnesium (*E*), phosphorus (*F*), calcium (*G*) and iron (*H*).

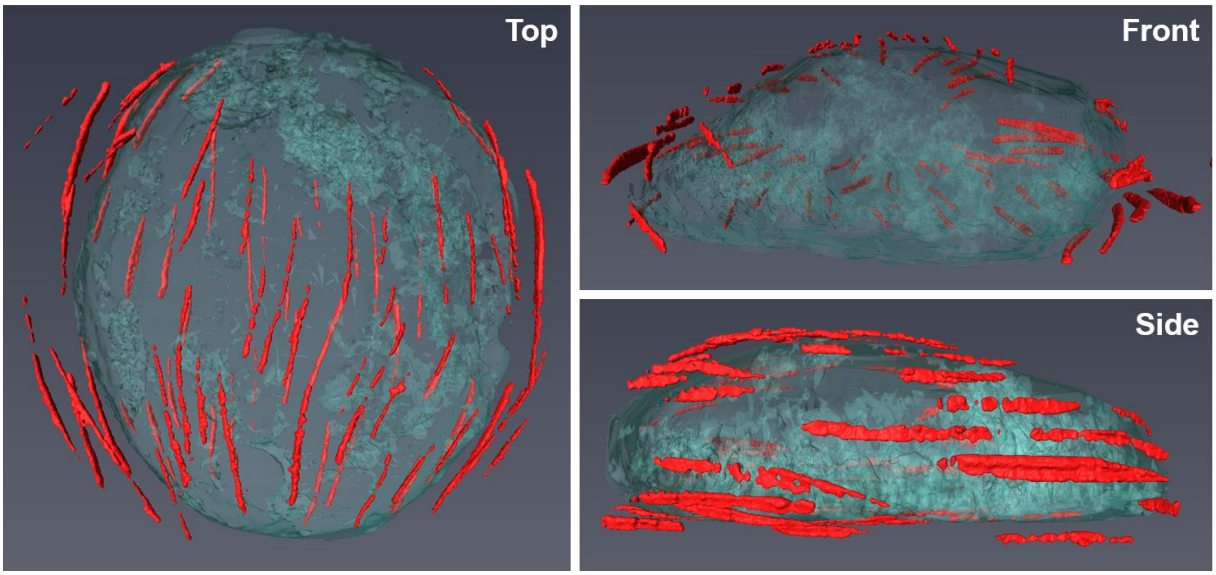

Fig. S5. 3-D volume reconstruction of magnetosome chains (red) and protistan host (cyan) from X-ray tomography (cryo-SXT) data.

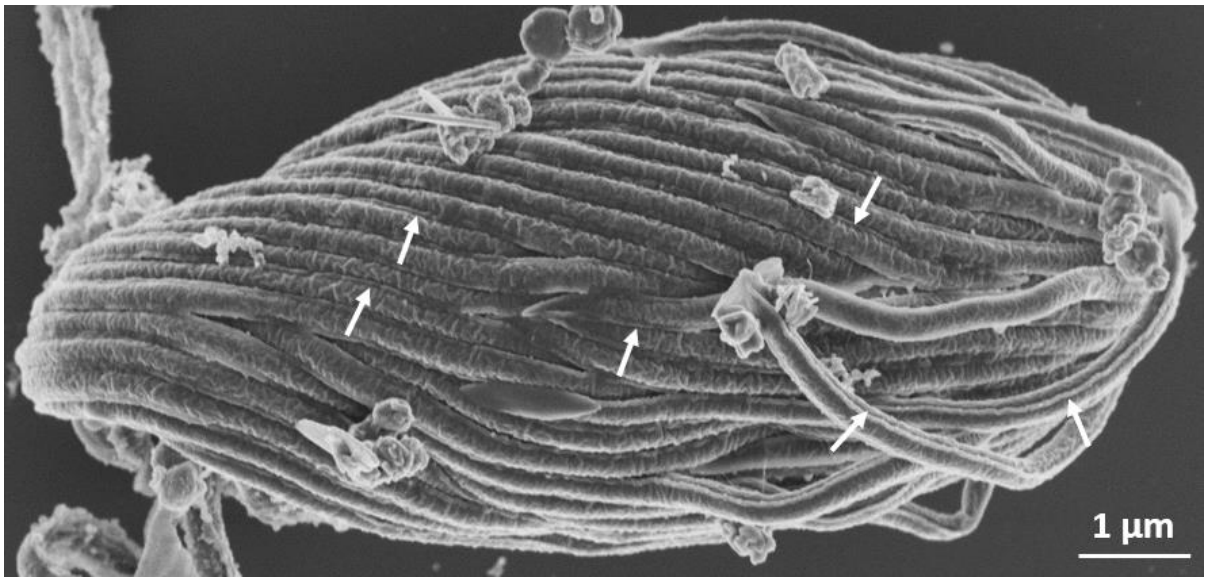

Fig. S6. SEM image of a MHB prepared using a critical-point drying approach showing the presence of lines between each neighbor magnetic ectosymbiotic bacteria or two lines on the side of each bacteria detached from the host (i.e. white arrows). These lines correspond to the wing-like structures observed on transversal thin-sectioned bacteria observed on TEM (Fig. 4C-E). Note that although it was fixed, this holobiont suffers from the preparation explaining the partial detachment and misalignment of some ectosymbiotic bacteria from their host.

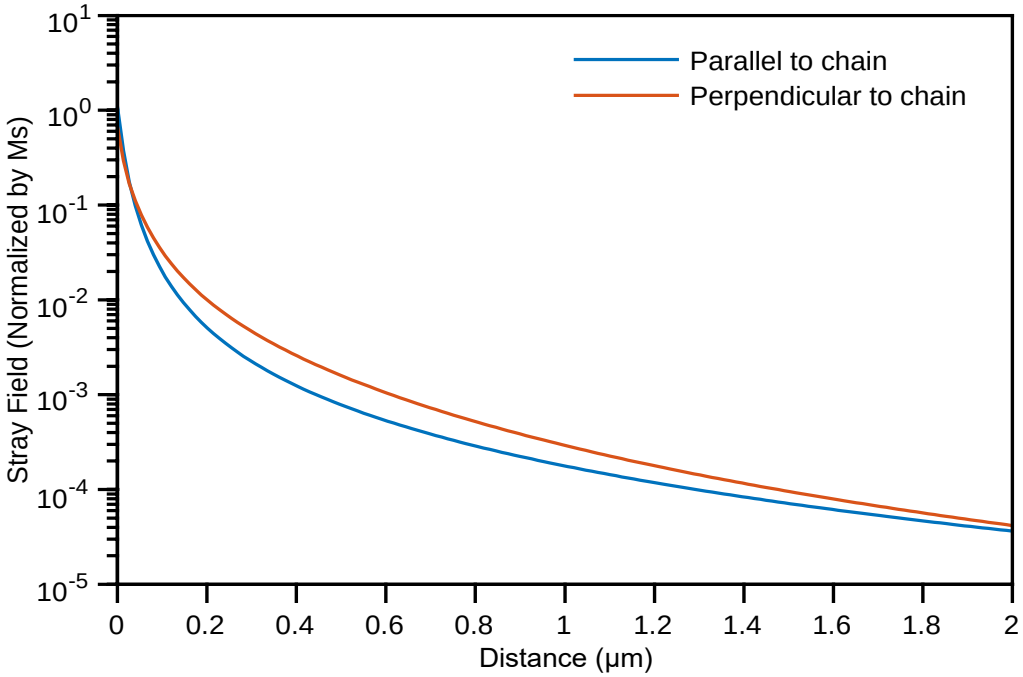

Fig. S7. Micromagnetic simulations of a modelled magnetosome chain from MHB (25 rhomboidal dodecahedral particles with a mid-sphere diameter of 60 nm and 10 nm spacing between particles) showing the stray fields adjacent to the chain.

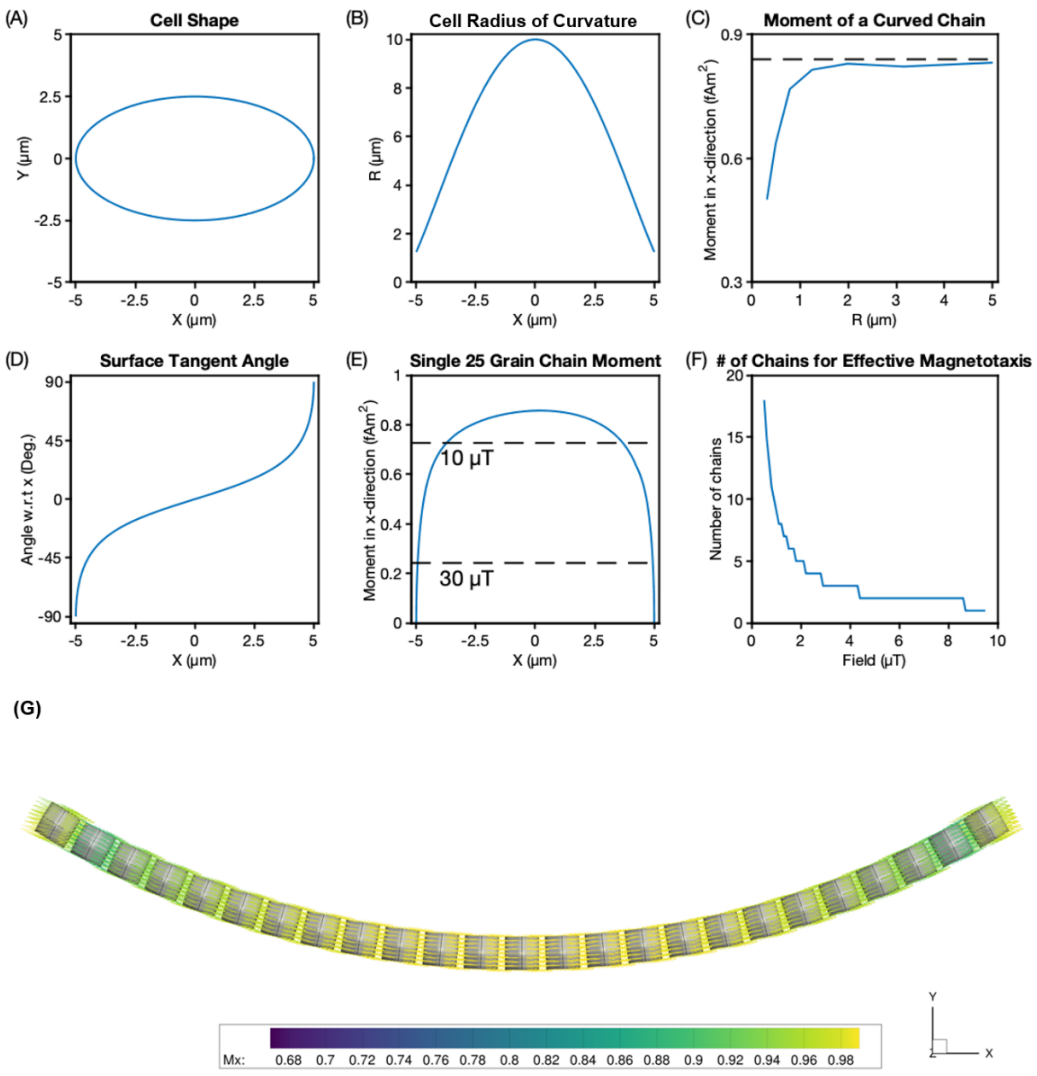

Fig. S8. Calculations to determine the net moment of a protist cell with chains of 25 rhomboidal dodecahedral magnetosomes (with a mid-sphere diameter of 60 nm and spacing of 10 nm) at various degrees of chain curvature. (*A*) The dimensions of a prolate cross-section of a protist cell. (*B*) The radius of curvature of the cell as a function of long axis position. (*C*) The net x-direction magnetic moment of the magnetosome chain with increasing radius of curvature (Note: as the radius increases the degree of chain bending decreases). (*D*) The angle of the surface tangent with respect to the x-direction. (*E*) The net x-direction moment of a single magnetosome chain as a function of long axis position accounting for the cell curvature and tangential angle with respect to the x-direction. The horizontal dashed lines indicate the magnetic moments at which the characteristic timescales of magnetic torque rotation and Brownian motion (at 20 °C) are equal in fields of 10 or 30 µT. (*F*) The minimum number of chains for effective magnetotaxis as a function of field. One chain near the middle of the cell is sufficient to overcome Brownian motion in ~10 µT and 2-3 chains would be sufficient to impart a significant magnetotactic advantage over other similarly sized organisms. In extremely weak fields (~1 µT) about nine chains are required to overcome Brownian effects. (*G*) An example micromagnetic calculation for the chain of 25 magnetosomes. The chain is curved around a circle of radius 1.25 µm. Magnetic moment vectors are colored according to percentage of maximum alignment (0.00 to 1.00) with the x-direction (Mx).

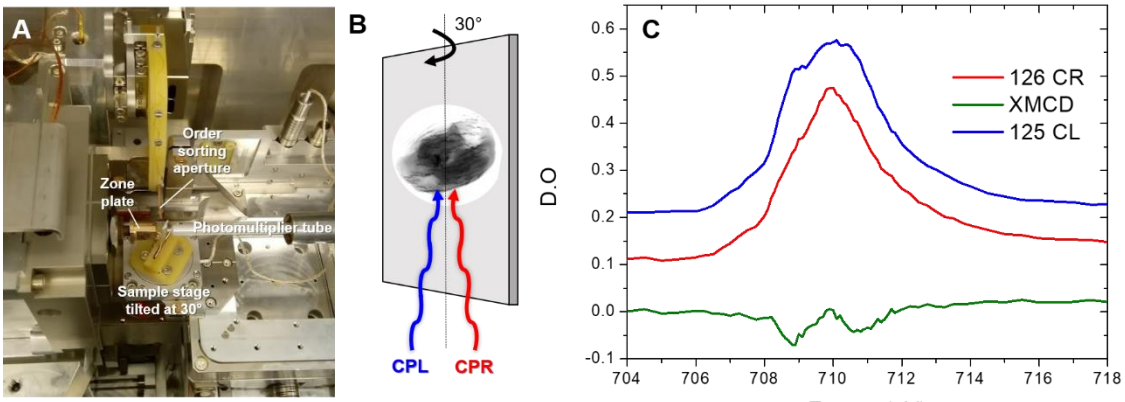

Fig. S9. (*A*) Scanning transmission X-ray microscopy (STXM) experimental sample environment for X-ray magnetic circular dichroism (XMCD) measurement. (*B*) Depiction of 30 deg tilt to measure the intrinsic XMCD signal of the MHB sample, where the magnetosome chains are perpendicular to the axis of rotation. (*C*) Example of Fe L_3-edge XAS spectra recorded with right (CPR)- and left (CPL)-circularly polarized X-rays with the difference spectra or XMCD signal. XAS spectra highly resemble magnetite and magnetosomes materials as found in other STXM-XMCD studies (1, 2).

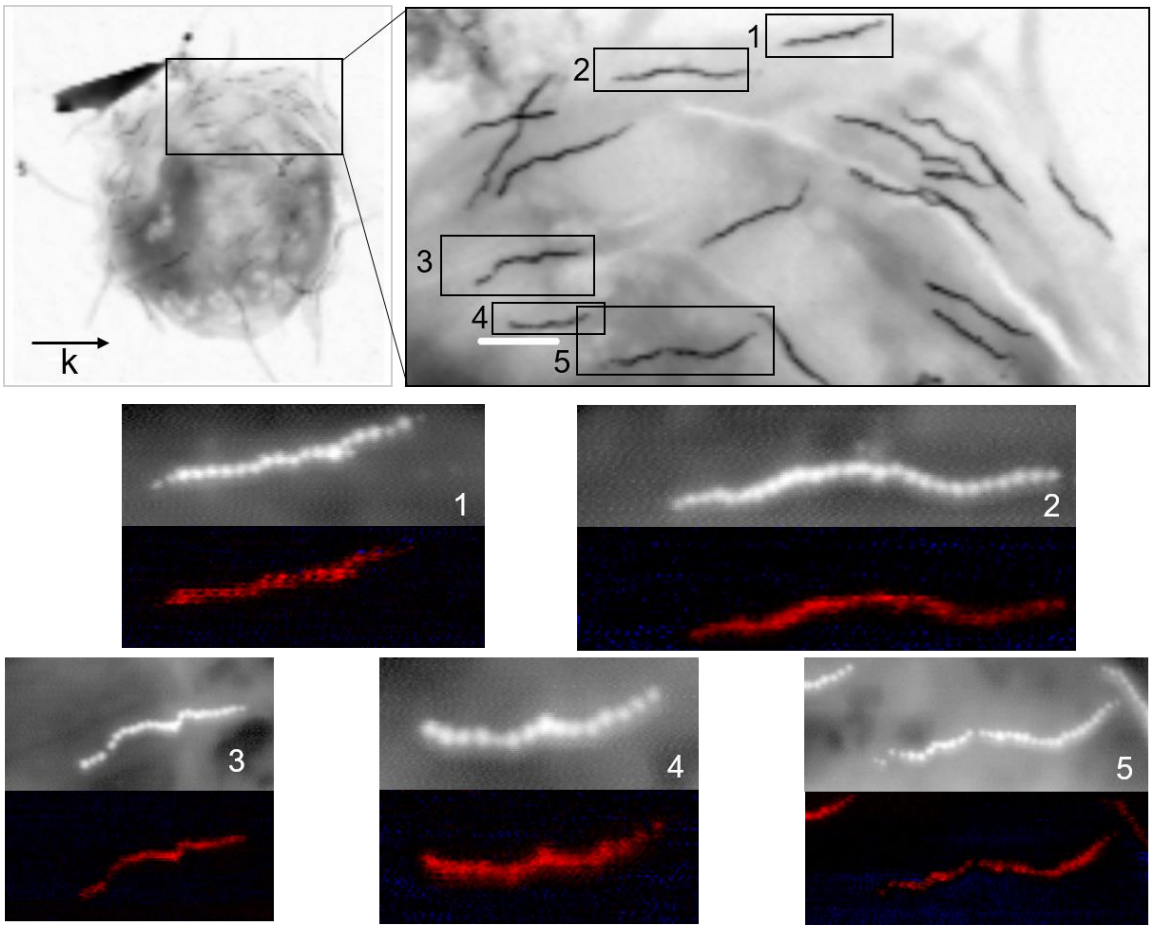

Fig. S10. Scanning transmission X-ray microscopy (STXM) images of unfixed MHB at 710 eV (above) with X-ray magnetic circular dichroism (XMCD) maps (OD-corrected and CPL-CPR images at 708.8 eV) of individual magnetosome chains (below).

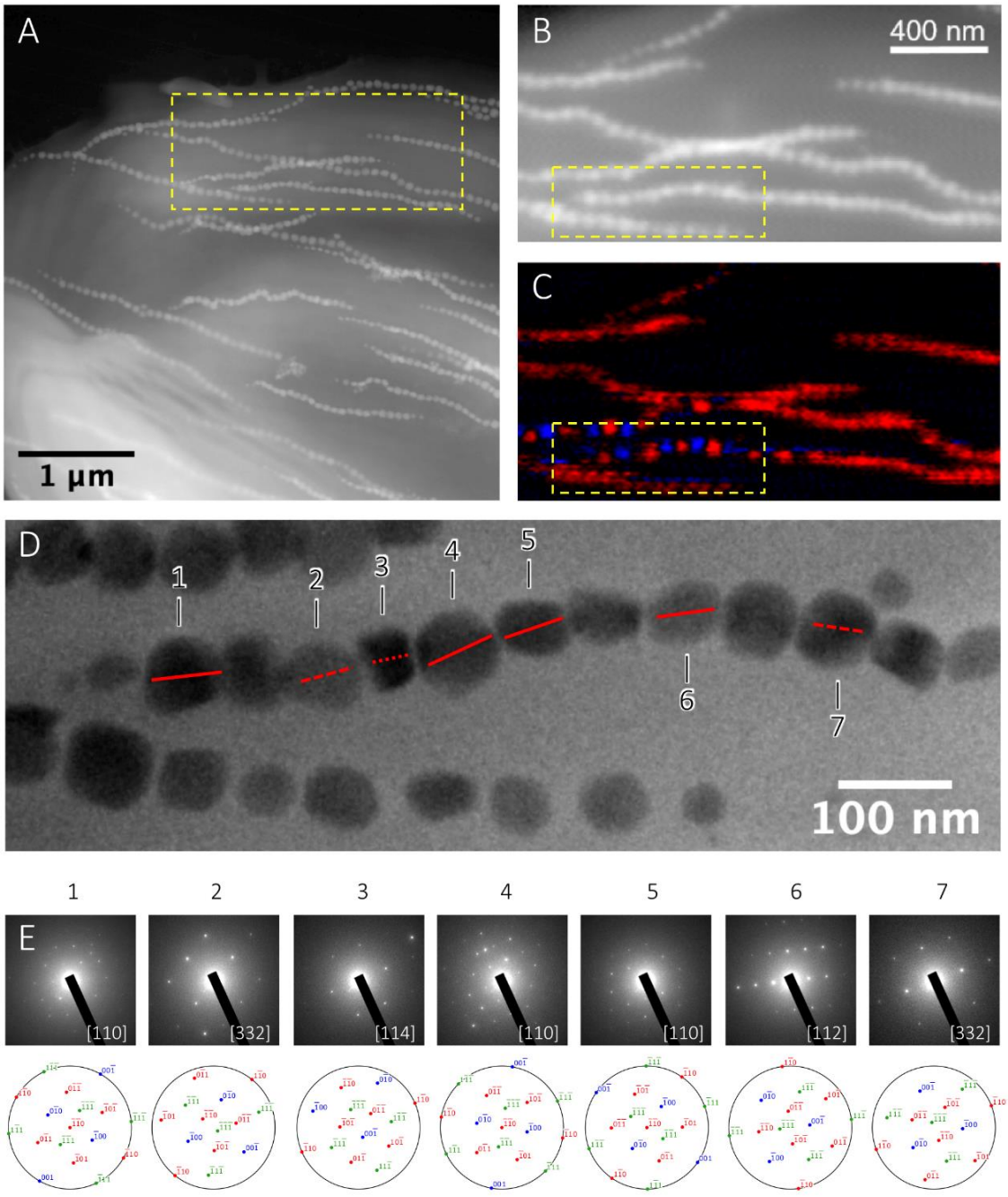

Fig. S11. (*A-B*) Scanning transmission electron microscopy high-angle annular dark field (STEM-HAADF) images of the region where individual magnetite nanocrystal magnetic dipoles invert (Fig. 5A (top left) and C (top right)) showing the morphology and organization of magnetosomes. Dashed frames indicate the regions further analyzed. (*C*) Difference maps of circular polarization left (CPL) at 708.8 eV showing two magnetosome chains extremity with inversion of individual magnetic dipole direction.. (*D*) Transmission electron microscope bright-field (TEM-BF) image of the dashed region in (*C*) containing magnetosomes with inversion of individual magnetic dipole direction. Red lines across selected magnetosome particles indicate the <111> direction as determined in (*E*) from single particle diffraction, with fast Fourier transform (FFT) and stereographic projections shown below for each particle.

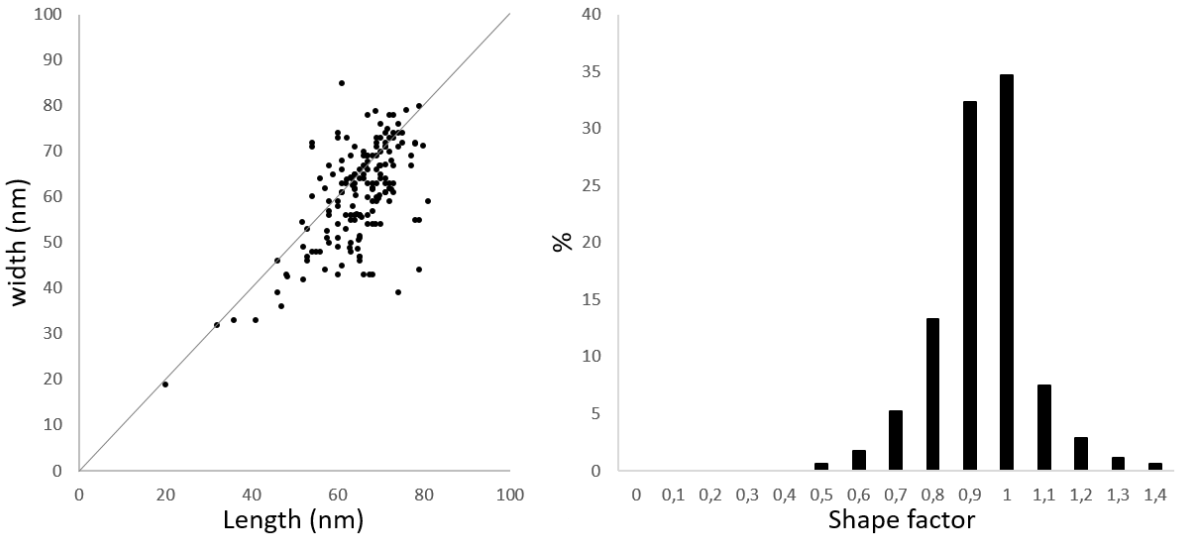

Fig. S12. Width versus length and crystal shape factor distribution of magnetic ectosymbiotic bacteria showing a general trend of cuboctahedral particles. 173 magnetosomes from several ectosymbionts and three different MHB were measured, considering the size of the particle parallel to the chain, the length and the size of the particle perpendicular to the chain, the width. An average length and width of 65 ± 9 nm and 60 ± 11 nm, respectively, was found. The shape factor (width/length) was 0.93 ± 0.13. These results are consistent with analyses of cuboctahedral/prismatic particles from environmental or cultivated MTB (3–6).

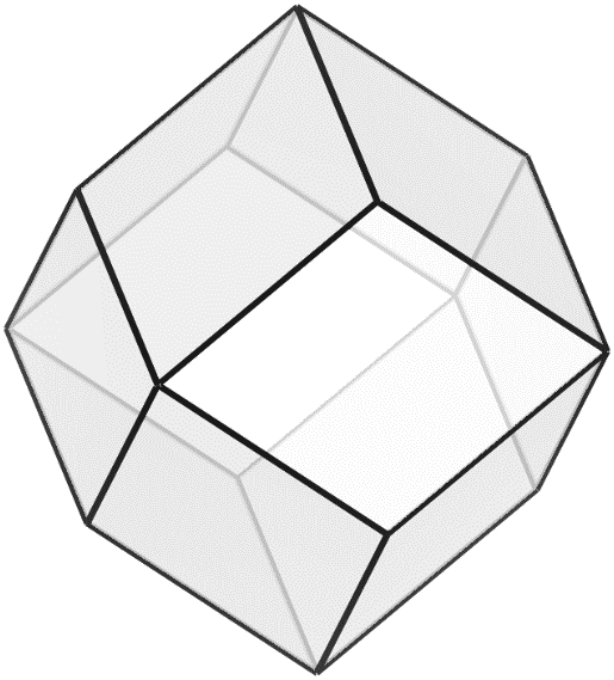

908

909 **Fig. S13.** Proposed crystallographic shape of magnetite nanocrystals as measured by high-resolution
910 transmission electron microscopy (Fig. 6, Fig. S14 and S15).

911

912

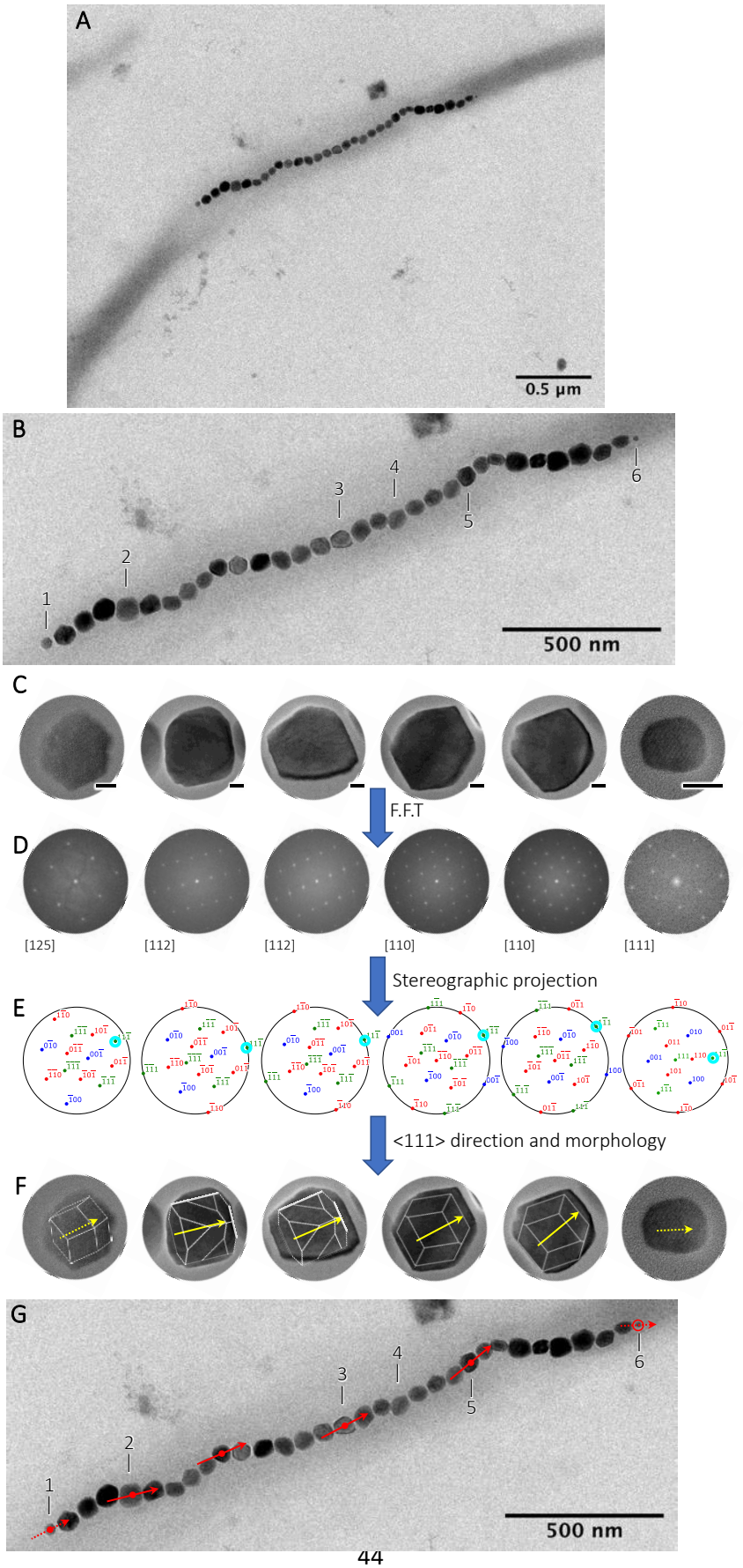
A
0.5 μm
B
1
2
3
4
5
6
500 nm
C
F.F.T
D
[125]
[112]
[112]
[110]
[110]
[111]
Stereographic projection
E
<111> direction and morphology
F
G
1
2
3
4
5
6
500 nm

Fig. S14. Crystallography of the prismatic/cuboctahedral magnetite particles produced by magnetic ectosymbiotic bacteria. (*A*) Transmission electron microscope bright-field (TEM-BF) image of a magnetic ectosymbiotic bacterium detached from its host and (*B*) single magnetosome chain. (*C*) High-resolution transmission electron microscopy (HR-TEM) images of the crystals annotated 1-6 in (*B*) scale bars 10 nm. (*D*) Fast Fourier transform (FFT) patterns of HR-TEM indexed with the magnetite structure (spacegroup $Fm\bar{3}m$, a = 8.04 Å). (*E*) Stereographic projection oriented with respect to the orientation inferred from (*D*) using SingleCrystal software, the 111 pole are outlined by a cyan circle. (*F*) Prismatic models drawn in white are superimposed to the image of the crystals. Yellow arrows indicate the <111> direction: solid arrows correspond to in-plane direction and dashed arrows are related to out-of-plane direction. The <111> directions and the orientation of the models were deduced from the stereographic projections. (*G*) For each analyzed crystal, the <111> direction is superimposed to the magnetosome chain (red arrows) showing that their easy magnetization axis is aligned with the overall chain direction.

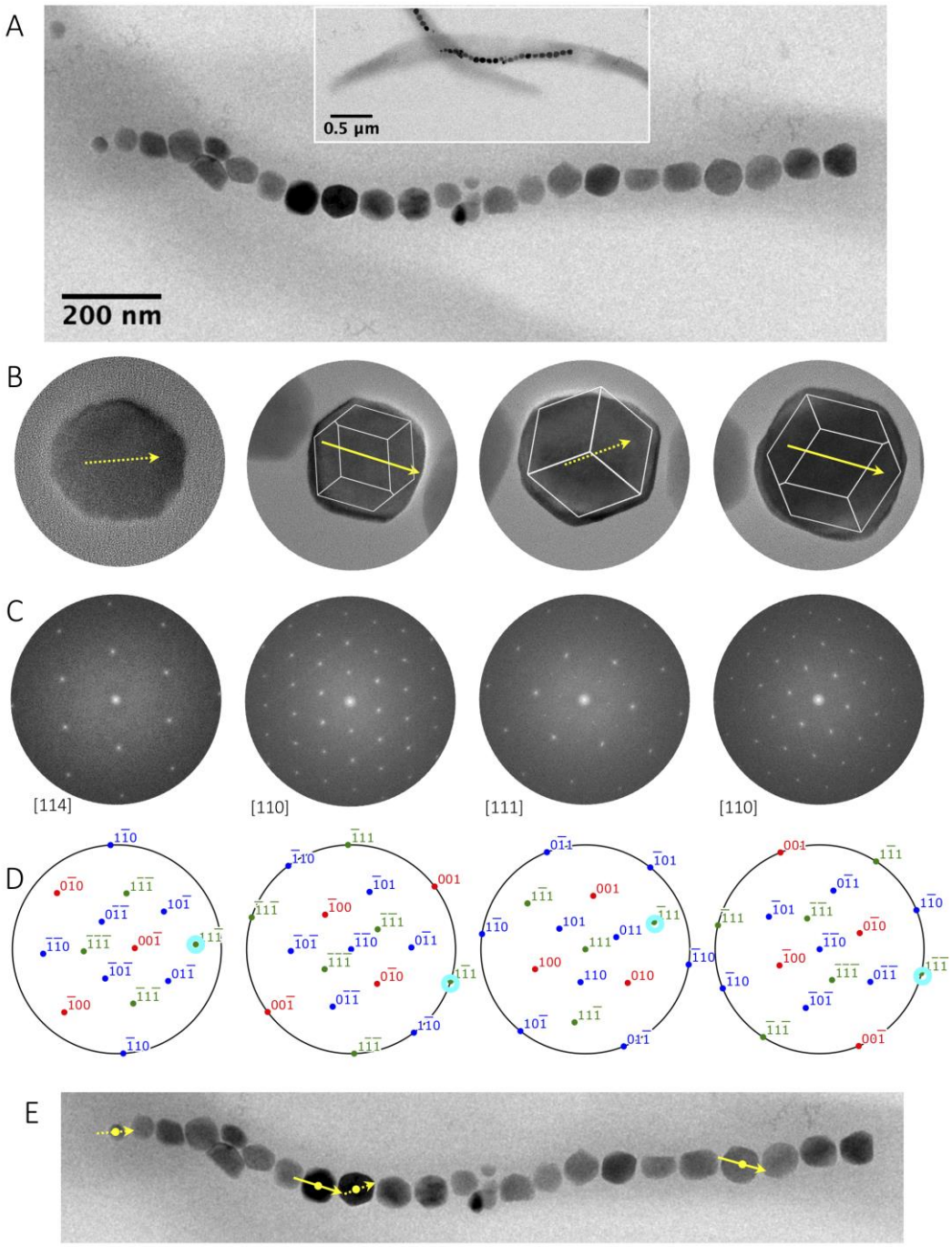

Fig. S15. Crystallography of the prismatic/cuboctahedral magnetite particles produced by magnetic ectosymbiotic bacteria. (*A*) TEM-BF image of a magnetic ectosymbiotic bacterium detached from its host. (*B*) HR-TEM images of four crystals with superimposed prismatic models drawn in white and yellow arrows to indicate the <111> direction (solid arrows are in-plane and dashed arrows out-of-plane). (*C*) FFT pattern of HR-TEM indexed with the magnetite structure (spacegroup $Fm\bar{3}m$, $a = 8.04$ Å). (*D*) Stereographic projection oriented with respect to the orientation inferred from (*C*) with the 111 pole outlined by a cyan circle. (*E*) For each analyzed crystal, the <111> direction is superimposed to the magnetosome chain (yellow arrows) showing that their easy magnetization axis is aligned with the overall chain direction.

References

1. L. Le Nagard, *et al.*, Magnetite magnetosome biomineralization in Magnetospirillum magneticum strain AMB-1: A time course study. *Chem. Geol.* **530**, 119348 (2019).

2. L. Marcano, *et al.*, Magnetic Anisotropy of Individual Nanomagnets Embedded in Biological Systems Determined by Axi-asymmetric X-ray Transmission Microscopy. *ACS Nano* (2022) https:/doi.org/10.1021/acsnano.1c09559.

3. A. Isambert, N. Menguy, E. Larquet, F. Guyot, J.-P. Valet, Transmission electron microscopy study of magnetites in a freshwater population of magnetotactic bacteria. *Am. Mineral.* **92**, 621–630 (2007).

4. S. Mann, R. B. Frankel, R. P. Blakemore, Structure, morphology and crystal-growth of bacterial magnetite. *Nature* **310**, 405–407 (1984).

5. B. Devouard, *et al.*, Magnetite from magnetotactic bacteria: Size distributions and twinning. *Am. Mineral.* **83**, 1387–1398 (1998).

6. M. Pósfai, C. T. Lefèvre, D. Trubitsyn, D. A. Bazylinski, R. B. Frankel, Phylogenetic significance of composition and crystal morphology of magnetosome minerals. *Front. Microbiol.* **4**, 344 (2013).